

The HARPS search for southern extra-solar planets [★]

XL. Searching for Neptunes around metal-poor stars

J. P. Faria^{1,2}, N. C. Santos^{1,2}, P. Figueira¹, A. Mortier³, X. Dumusque⁴, I. Boisse⁵, G. Lo Curto⁶, C. Lovis⁷, M. Mayor⁷, C. Melo⁶, F. Pepe⁷, D. Queloz^{7,8}, A. Santerne¹, D. Ségransan⁷, S. G. Sousa¹, A. Sozzetti⁹, and S. Udry⁷

¹ Instituto de Astrofísica e Ciências do Espaço, Universidade do Porto, CAUP, Rua das Estrelas, PT4150-762 Porto, Portugal
e-mail: joao.faria@astro.up.pt

² Departamento de Física e Astronomia, Faculdade de Ciências, Universidade do Porto, Rua Campo Alegre, 4169-007 Porto, Portugal

³ SUPA, School of Physics and Astronomy, University of St Andrews, St Andrews KY16 9SS, UK

⁴ Harvard-Smithsonian Center for Astrophysics, 60 Garden Street, Cambridge, MA 02138, USA

⁵ Aix Marseille Université, CNRS, LAM (Laboratoire d'Astrophysique de Marseille) UMR 7326, 13388, Marseille, France

⁶ European Southern Observatory, Casilla 19001, Santiago, Chile

⁷ Observatoire de Genève, Université de Genève, 51 ch. des Maillettes, CH-1290 Sauverny, Switzerland

⁸ Institute of Astronomy, University of Cambridge, Madingley Road, Cambridge, CB3 0HA, UK

⁹ INAF - Osservatorio Astrofisico di Torino, Via Osservatorio 20, I-10025 Pino Torinese, Italy

Received October 8, 2015; accepted January 7, 2016

ABSTRACT

Context. Stellar metallicity – as a probe of the metallicity of proto-planetary disks – is an important ingredient for giant planet formation, likely through its effect on the timescales in which rocky/icy planet cores can form. Giant planets have been found to be more frequent around metal-rich stars, in agreement with predictions based on the core-accretion theory. In the metal-poor regime, however, the frequency of planets, especially low-mass planets, and how it depends on metallicity are still largely unknown.

Aims. As part of a planet search programme focused on metal-poor stars, we study the targets from this survey that were observed with HARPS on more than 75 nights. The main goals are to assess the presence of low-mass planets and provide a first estimate of the frequency of Neptunes and super-Earths around metal-poor stars.

Methods. We perform a systematic search for planetary companions, both by analysing the periodograms of the radial-velocities and by comparing, in a statistically-meaningful way, models with an increasing number of Keplerians.

Results. A first constraint on the frequency of planets in our metal-poor sample is calculated considering the previous detection (in our sample) of a Neptune-sized planet around HD175607 and one candidate planet (with an orbital period of 68.42 d and minimum mass $M_p \sin i = 11.14 \pm 2.47 M_{\oplus}$) for HD87838, announced in the present study. This frequency is determined to be close to 13% and is compared with results for solar-metallicity stars.

Key words. methods: data analysis – planetary systems – surveys – stars: individual: HD87838 – techniques: radial velocities

1. Introduction

More than 600 exoplanets were discovered and many others confirmed using radial-velocity (RV) observations (www.exoplanet.eu, Schneider et al. 2011). The method is more sensitive to massive planets orbiting close to their stars since Neptune- and Earth-mass planets induce very small amplitude radial-velocity signals, often at the level of the current observational uncertainties of 1 m s^{-1} and smaller. In addition, stellar activity can induce false-positive signals that mimic and mask the radial velocity signature of a low-mass planet (e.g. Bonfils et al. 2007; Robertson & Mahadevan 2014; Santos et al. 2014). Only with very high precision Doppler spectroscopy and dense sampling one is able to detect these planets (e.g. Dumusque et al. 2012; Hatzes 2014) and to push the detection limits in the direction of a possibly habitable Earth-like planet, the same stars must be followed for a very long time.

[★] Based on observations collected at ESO facilities under programs 082.C-0212, 085.C-0063, 086.C-0284, and 190.C-0027 (with the HARPS spectrograph at the ESO 3.6-m telescope, La Silla-Paranal Observatory).

The increasing number of detected planets provides constraints for models of planet formation and evolution (e.g. Udry & Santos 2007; Ida & Lin 2004; Mordasini et al. 2009). In particular, the metallicity and, in general, the chemical abundances of the host star, are now known to be a key ingredient in planet formation (Ida & Lin 2004; Mordasini et al. 2015). According to the core-accretion theory, proto-planetary disks with higher metallicity are able to form rocky/icy cores in time for runaway accretion to lead to the formation of a giant planet before disk dissipation occurs. In lower metallicity disks, the cores do not grow fast enough to accrete gas in large quantities before disk dissipation occurs, implying a lower fraction of giant planets.

Gonzalez (1997) showed the first observational hints for a correlation between the presence of giant planets and metallicity. As more and more planets were discovered, this correlation was solidly confirmed: it is more likely to detect a giant planet orbiting a metal-rich star (Santos et al. 2004; Fischer & Valenti 2005; Sousa et al. 2011b). This result was also confirmed in data from transit surveys (e.g. Buchhave et al. 2012). Furthermore, it is also now known that the metallicity, or even specific chemical abundance ratios, can have a strong impact on the planet for-

mation efficiency, composition, and architecture (Guillot et al. 2006; Adibekyan et al. 2013, 2015; Dawson et al. 2015; Santos et al. 2015).

Because giant planets are more frequent around metal-rich stars, several RV surveys became biased towards metal-rich samples (Tinney et al. 2002; Fischer & Valenti 2005; Melo et al. 2007; Jenkins et al. 2013a). Nevertheless, some programmes focused on the metal-poor regime, and tried to determine the frequency of giant planets orbiting metal-poor stars, and the metallicity limit below which no giant planets can be observed (Sozzetti et al. 2009; Santos et al. 2011; Mortier et al. 2012, 2013). Until recently, however, these programs focused on the search for massive, giant planets.

Neptune-mass planets, in contrast, have been found to have a relatively flat metallicity distribution (Udry et al. 2006; Sousa et al. 2008, 2011b; Neves et al. 2013). In systems with only hot Neptunes, the metallicity distribution actually becomes slightly metal-poor (Mayor et al. 2011; Buchhave et al. 2012). These results are supported by theoretical models which predict lower-mass planets to be common around stars with a wide range of metallicities. One should note here the works of Wang & Fischer (2014) and Buchhave & Latham (2015), who find conflicting results over the existence of a universal planet-metallicity correlation extending to the terrestrial planets, and Adibekyan et al. (2012) who show that, in the metal-poor regime, planets are more prevalent on α -enhanced stars (i.e. of higher global metallicity).

The number of detected low-mass planets orbiting metal-poor stars is nevertheless still small. In an effort to detect these planets and explore the low metallicity regime, our team started a Large Program with HARPS to follow a sample of about 100 metal-poor stars. The program and sample were presented in Santos et al. (2014), to which we point the reader for more details. The main goal of the survey is to derive observational constraints on the frequency of Neptunes and super-Earths in the metal-poor regime. These estimates will be compared with the ones from the HARPS-GTO program (Mayor et al. 2011) which searched for very low mass planets orbiting a sample of solar-neighbourhood stars (thus with solar metallicities). When combined, the two surveys will set important constraints for planet formation and evolution models and help in providing an estimate of the frequency of planets in our Galaxy.

This paper presents the analysis of the stars in the metal-poor sample that were observed on more than 75 nights. Some of these stars now have precise radial velocity observations covering a baseline of over ten years. In Sect 2 we present the stellar parameters for these stars and their radial-velocity observations. The method used to search for Keplerian signals is outlined in Sect. 3 and in Sect 4 the results of its application are presented. Section 5 presents a simple comparison of the model selection criteria we consider and detection limits for individual stars are derived in Sect. 6. A first constraint on the occurrence of planets in this sample and our conclusions are presented in Sect. 7.

2. Sample and Observations

Our complete sample of metal-poor stars contains 109 targets, chosen from a survey for giant planets orbiting metal-poor stars (Santos et al. 2007) and a programme to search for giant planets orbiting a volume-limited sample of FGK dwarfs (Naef et al. 2007). The criteria for the definition of this sample are detailed in Santos et al. (2014). Stellar parameters were derived from the complete sample from a set of high-resolution HARPS spectra (Sousa et al. 2011a; Santos et al. 2014).

In this work we analyse those stars which, up to December 2014, were observed on more than 75 nights. This number of nights, though not strictly motivated, means that in the worst case scenario we have six data points per parameter, for a model with two planets. A total of 15 stars meet this criteria. In Table 1 we present the stellar parameters for this subsample.

The activity level of the stars, denoted here by the weighted average of the $\log R'_{\text{HK}}$ values (Noyes et al. 1984b), was derived from the analysis of the CaII H and K lines in the HARPS spectra (e.g. Santos et al. 2000; Lovis et al. 2011). Estimates for the rotation period of each star were derived from the activity-rotation calibrations of Noyes et al. (1984b) and Mamajek & Hillenbrand (2008). The typical error bar on these estimates, computed from the dispersion in the $\log R'_{\text{HK}}$ time series, is of the order of the difference between the estimates from the two calibrations. For HD31128, the rotation period derived in this way is around 2.8 d. The very low metallicity of this star, however, places it outside the calibration range of the $\log R'_{\text{HK}}$ flux calibration, and of the adopted activity-rotation relations. This renders the rotation period estimate uncertain, and we chose to omit it from the table.

Table 2 shows the number of nights each star was observed, the mean error bar $\bar{\sigma}_i$, and the weighted standard deviation of the radial velocities s_{RV} . The ratio of the two latter quantities gives an indication of whether the radial-velocities vary in excess of the internal errors, and by how much. This table also shows the baseline of observations.

The distributions of metallicity, effective temperature and surface gravity of the full sample and of the 15 stars studied here are shown in Fig. 1. By selecting stars based on the number of observations, one can introduce biases that depend on the criteria used for scheduling observations. From the distributions in Fig. 1, we do not see a clear bias towards warmer or more evolved stars, which may show more significant (stellar) variability. The sub-sample can nevertheless be biased in favour of stars hosting low mass planets, since these stars will also show more significant variability. This can have an impact on our determination of the planet frequency (Sect. 7), although it is difficult to determine to which extent. Regarding metallicity, the subsample is representative of the overall distribution but does not span the complete metallicity range.

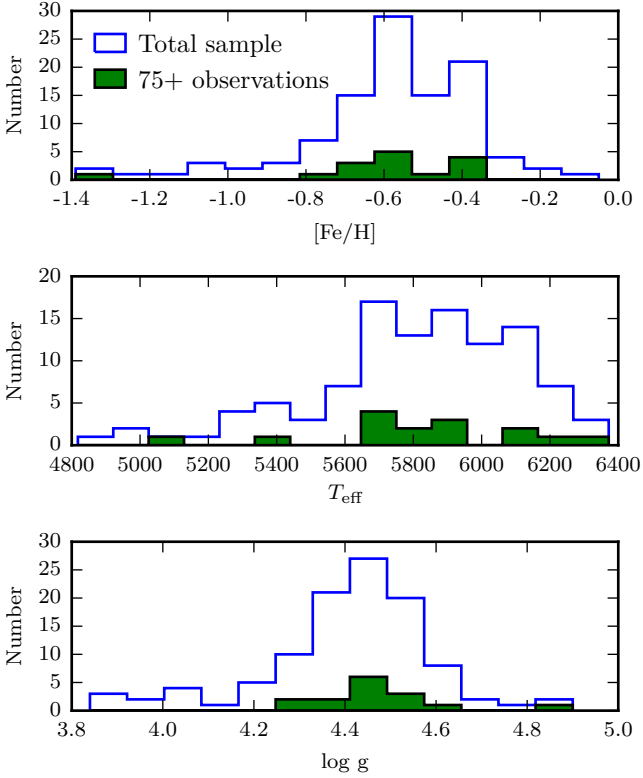
For these 15 stars, we analyse a total of 1540 radial velocity measurements obtained using the HARPS spectrograph at the 3.6m ESO telescope (La Silla-Paranal Observatory). All observations were reduced with the HARPS pipeline (version 3.5), where the radial velocities are obtained by performing a cross-correlation of the observed spectrum with a numerical mask (Baranne et al. 1996; Pepe et al. 2002).

For the first measurements (obtained before the present Large Program and still within the HARPS GTO program), the exposure times were not long enough to average out the noise coming from stellar oscillations and the radial velocities had a limiting precision of around 2 m s^{-1} . The observing strategy was since revised by setting exposure times to 900 s, resulting in a precision of the order of 1 m s^{-1} . With the start of the Large Program, in October 2012, we aimed at obtaining more than one spectrum of the star in a given night, separated by several hours.

We use nightly binned data in our analysis, thus focusing on signals with periods longer than one night. The objective of this strategy is to minimize the impact of granulation phenomena on the radial velocities and improve the planetary detection limits (see Dumusque et al. 2011c). We note, however, that this observing strategy has some caveats since it has been designed for and tested in stars with solar metallicities and its optimality is not guaranteed for metal-poor stars. Also, considering the binned

Table 1. Stellar parameters for each of the 15 stars studied here. The table lists the mass, effective temperature, surface gravity, metallicity, B-V color, activity level, and estimated rotation period.

Star	Mass [M_{\odot}]	T_{eff} [K]	$\log g$ [cgs]	[Fe/H]	$B - V$	$\log R'_{HK}$	$P_{\text{rot}}^{(a)}$ [days]
HD224817	0.98 ± 0.06	5894 ± 22	4.36 ± 0.02	-0.53 ± 0.02	0.55	-4.96	13.0 / 13.5
HD21132	1.05 ± 0.07	6243 ± 34	4.60 ± 0.05	-0.37 ± 0.02	0.49	-4.90	7.2 / 7.3
HD22879	0.88 ± 0.06	5884 ± 33	4.52 ± 0.03	-0.81 ± 0.02	0.56	-4.91	12.8 / 13.1
HD31128	0.79 ± 0.05	6096 ± 67	4.90 ± 0.05	-1.39 ± 0.04	0.41	-4.88 ^(b)	–
HD41248	0.94 ± 0.06	5713 ± 21	4.49 ± 0.03	-0.37 ± 0.01	0.61	-4.89	18.2 / 18.4
HD56274	0.90 ± 0.06	5734 ± 22	4.51 ± 0.03	-0.54 ± 0.02	0.57	-4.85	13.3 / 13.3
HD79601	0.94 ± 0.06	5834 ± 25	4.37 ± 0.04	-0.60 ± 0.02	0.53	-4.95	11.0 / 11.4
HD87838	1.03 ± 0.07	6118 ± 33	4.47 ± 0.03	-0.40 ± 0.02	0.52	-4.92	9.7 / 9.9
HD88725	0.87 ± 0.06	5654 ± 17	4.49 ± 0.03	-0.64 ± 0.01	0.60	-4.90	17.3 / 17.6
HD111777	0.87 ± 0.06	5666 ± 19	4.46 ± 0.03	-0.68 ± 0.01	0.61	-4.91	18.7 / 19.1
HD114076	0.80 ± 0.06	5069 ± 52	4.32 ± 0.09	-0.47 ± 0.04	0.82	-4.98	41.4 / 43.4
HD119173	0.96 ± 0.06	5779 ± 44	4.26 ± 0.04	-0.62 ± 0.03	0.56	-4.87	12.7 / 12.8
HD119949	1.09 ± 0.07	6359 ± 36	4.47 ± 0.04	-0.41 ± 0.02	0.45	-4.96	5.0 / 5.2
HD126793	0.92 ± 0.06	5910 ± 31	4.46 ± 0.03	-0.71 ± 0.02	0.52	-4.92	9.8 / 10.0
HD175607	0.81 ± 0.05	5392 ± 17	4.51 ± 0.03	-0.61 ± 0.01	0.70	-4.92	28.9 / 29.7

Notes. ^(a) The two values are estimated from the $\log R'_{HK}$ measurements using the calibrations from Noyes et al. (1984b) and Mamajek & Hillenbrand (2008), respectively. ^(b) After removing the observation at $BJD = 2455304.48$ for which the $\log R'_{HK}$ value was not calculated.

Fig. 1. Metallicity, effective temperature and surface gravity distributions for the full metal-poor sample (blue histograms) and the 15 stars observed on more than 75 different nights (green filled histograms).

data means we cannot assess the presence of shorter period planets (e.g. Dawson & Fabrycky 2010; Hatzes 2014; Grunblatt et al. 2015).

Table 2. Number of individual night observations, average RV errorbar, weighted standard deviation of the RV measurements and timespan for each of the targets.

Star	N	$\bar{\sigma}_i$ [m s^{-1}]	s_{RV} [m s^{-1}]	Δt [days]
HD224817	100	1.15	1.98	4044
HD21132	85	2.25	2.65	3935
HD22879	80	0.81	1.60	4053
HD31128	171	3.57	3.58	4081
HD41248	160	1.26	3.41	3737
HD56274	161	0.80	2.70	4046
HD79601	79	1.00	1.77	3761
HD87838	87	1.34	2.36	3983
HD88725	90	0.79	2.35	3941
HD111777	79	1.09	1.60	3756
HD114076	77	1.41	1.87	3727
HD119173	98	1.59	1.62	2959
HD119949	81	1.50	2.23	3614
HD126793	79	1.28	1.90	3595
HD175607	113	1.08	2.62	3713

3. Methodology

As a first step in the analysis of each star, and as is standard when searching for planets in RV data, we compute the generalised Lomb-Scargle (GLS) periodogram (Zechmeister & Kürster 2009) of the radial velocities and search for significant peaks. The significance of a peak is evaluated by the false alarm probability (FAP) estimated with a bootstrap permutation procedure, first devised by Murdoch et al. (1993); see also Endl et al. (2001); Mortier et al. (2012). The RV measurements and errorbars are (together) randomly redistributed, with repetition, keeping the time-stamps of observations fixed. For each randomization, a new GLS periodogram is computed and its maximum power is compared with the original periodogram, thus obtaining the FAP levels. After repeating this process 1000 times, we show the estimated 1% and 0.1% FAP levels.

If any periodogram peak is deemed significant, we proceed with the analysis of the RV data together with other activity proxies to try and determine the nature of the signal. We will focus on the FWHM of the HARPS CCF and the $\log R'_{\text{HK}}$ proxy as the most reliable indicators of activity, even though we have also analysed other indicators. It may also be that a signal is present in the data which was created by a planet with a moderately high eccentricity. The standard GLS periodogram (which searches for sinusoidal signals) is then not the best tool to recover it. Therefore, for the stars in which the periodogram does not show significant peaks, we still run a planet detection algorithm that compares the evidence for models with 0, 1 and 2 Keplerian signals (see below). For some stars which show evidence for a Keplerian signal, we further try to assert its nature.

As is now ubiquitous in the literature, our model for the radial-velocity observations v_i is described by a Gaussian sampling distribution

$$v_i | M_n \sim \mathcal{N}(V_0 + V_n(t_i, \theta), \sigma_i^2 + s^2) \quad (1)$$

where M_n represents a model with n planets, V_0 is a constant offset, $V_n(t_i, \theta)$ is the radial-velocity shift caused by n orbiting planets, which depends on time t_i and the planets' orbital parameters θ . The parameter s is an extra ‘‘jitter’’ term, added in quadrature to the total measurement uncertainties σ_i , which allows for additional white noise to be taken into account.

We assume each planet induces a Keplerian signal $k(t)$, such that $V_n(t) = \sum_n k(t)$. This signal depends on the orbital period P , semi-amplitude K , eccentricity e , argument of the periastron ω and time of periastron passage T_0 (e.g. Perryman 2014, chap. 2). When $n = 0$ we have $V_n = 0$ by definition.

To infer the number of Keplerians supported by a dataset $d = \{t_i, v_i, \sigma_i, i = 1, \dots, N\}$ we can calculate the marginal likelihood, or evidence E_n , for each of the models M_n :

$$E_n = p(d | M_n) = \int_{\Theta} p(d | \Theta, M_n) p(\Theta | M_n) d\Theta. \quad (2)$$

where $p(d | \Theta, M_n)$ is the likelihood function and $p(\Theta | M_n)$ the prior distribution for the parameters of the model. Note that Θ has different dimensions, depending on the value of n and corresponds to the full set of parameters to be marginalised over, $\Theta = \{V_0, s, \theta\}$. The likelihood is given by the product of the terms in Eq. (1) for every data point,

$$p(d | \Theta, M_n) = (2\pi)^{-N/2} \left[\prod_{i=1}^N (\sigma_i^2 + s^2)^{-1/2} \right] \times \exp \left\{ - \sum_{i=1}^N \frac{[v_i - V_0 - V_n(t_i, \theta)]^2}{2(\sigma_i^2 + s^2)} \right\} \quad (3)$$

The comparison between any pair of models is made by evaluating the associated odds ratio (e.g. Gregory 2010)

$$O_{ij} = \frac{p(M_i | d)}{p(M_j | d)} = \frac{p(M_i)}{p(M_j)} \cdot \frac{p(d | M_i)}{p(d | M_j)} \quad (4)$$

which simplifies to the ratio of the evidences when there is no prior preference for any model, that is, when $\frac{p(M_i)}{p(M_j)} = 1$. If there is a preference for a given model, it can be included directly in Eq. 4. In this work we chose to consider all models equally probable *a priori*. Kass & Raftery (1995) provide a qualitative scale for the interpretation of evidence ratio values.

To evaluate the difficult (multidimensional) integral in Eq. (2), we use the nested sampling algorithm (Skilling 2004) implemented in MULTINEST (Feroz et al. 2009, 2013). The key idea in nested sampling is to update a set of points, originally sampled from the prior, with new samples that are subject to a hard likelihood constraint. At each iteration, the algorithm progressively moves towards regions of higher likelihood. Each time a new sample is obtained, it is assigned a value $X \in [0, 1]$ representing the amount of prior mass estimated to lie at a higher likelihood than that of the discarded point¹. Assigning these X -value maps from the parameter space to $[0, 1]$ or, in other words, divides the prior volume into a large number of points with equal prior mass. In the new space, the prior becomes a uniform distribution and the likelihood is a decreasing function of X . Then, the evidence can be computed by simple quadrature. For further details, the reader is referred to Skilling (2004); Mukherjee et al. (2006); Sivia & Skilling (2006); Feroz et al. (2009).

Nested sampling also provides posterior samples for all parameters as a by-product. The necessary descriptive statistics can then be calculated from these samples. Estimating all the posterior distributions for a particular model is what we mean by *fitting* a Keplerian in the remainder of the paper. This algorithm has been tested and validated in the analysis of radial-velocity data by Feroz et al. (2011a,b) and Feroz & Hobson (2013).

Another way to approach the problem is to treat n (the number of Keplerians) itself as a free parameter of the model (so that it is part of Θ) and sample from its own posterior distribution, $p(n | d)$, to infer the number of Keplerians present in the data. We use the recent algorithm proposed by Brewer & Donovan (2015) to sample from this distribution. The method uses trans-dimensional birth-death moves, within the context of diffusive nested sampling (Brewer et al. 2011), and was found to give results comparable to MULTINEST, often with a smaller number of likelihood evaluations and less computation time. The same likelihood function and priors were used for both methods.

We further need to specify the priors for each of the parameters. It is through the priors that the Bayesian analysis can take into account the principle of parsimony and Occam's razor. What is important is not (only) the *number* of parameters in a model but instead the amount of support in their priors. This is the reason to choose uninformative and physically motivated priors.

The form and limits of the priors we use are shown in Table 3. A few of our choices merit further discussion. For the orbital periods, we use a Jeffrey's prior between 1d and the timespan of each dataset. Apart from HD56274 and HD175607, which are analysed separately, none of the stars show clear long-term trends that could suggest the presence of long period planets. We thus limit our search for periods shorter than the timespans, which are in fact very long already. The lower limit is due to our use of nightly binned observations. For the semi-amplitudes, a modified Jeffrey's prior is used, spanning the range 0 – 10 m s⁻¹ and with a ‘‘knee’’ at the mean error bar of each dataset. The choice of upper limit comes from the cuts used when defining the complete metal-poor sample (see Santos et al. 2014), which was stripped of stars showing large RV dispersions². The same arguments apply to the jitter prior. The prior for the orbital eccentricities was suggested by Kipping (2013) after an analysis of the population of known exoplanets. Priors for the other parameters are uniform between what we consider to be sensible limits.

¹ The prior mass element is $dX = p(\Theta | M_n) d\Theta$ such that $E = \int L dX$, with L the likelihood function.

² In our full sample, the highest radial-velocity rms is 4.1 m s⁻¹.

Table 3. Priors for the model parameters.

P [days]	$\mathcal{J}(1, \text{timespan})$
K [m s^{-1}]	$\mathcal{MJ}(\bar{\sigma}_i, 10)$
e	$\mathcal{B}(0.867, 3.03)$
ω [rad]	$\mathcal{U}(0, 2\pi)$
T_0 [days]	$\mathcal{U}(t_0, t_0 + \text{timespan})$
V_0 [m s^{-1}]	$\mathcal{U}(\min v_i, \max v_i)$
s [m s^{-1}]	$\mathcal{MJ}(\bar{\sigma}_i, 10)$

Notes. The average uncertainty $\bar{\sigma}_i$ is used in the priors for the semi-amplitude and jitter. The symbols have the following meaning: $\mathcal{J}(\cdot, \cdot)$ – Jeffreys prior with lower and upper limits; $\mathcal{MJ}(\cdot, \cdot)$ – Modified Jeffreys prior with knee and upper limit; $\mathcal{B}(\alpha, \beta)$ – Beta prior with shape parameters α and β ; $\mathcal{U}(\cdot, \cdot)$ – Uniform prior with lower and upper limits; See, e.g., Gregory (2007); Kipping (2013) for the mathematical forms of each distribution.

Model selection criteria other than the evidence can be more easily calculated using just the maximum-likelihood value \hat{L} and the total number of parameters in the model, N_{par} . When presenting our results, in Table 4, we include the values of the sample-corrected Akaike Information Criteria (AIC_C) and the Bayesian Information Criteria (BIC), calculated as described in Burnham & Anderson (2010):

$$AIC_C = -2 \ln \hat{L} + 2 N_{\text{par}} + \frac{2K(N_{\text{par}} + 1)}{n - N_{\text{par}} - 1}$$

$$BIC = -2 \ln \hat{L} + N_{\text{par}} \ln N$$

The preferred model, when using these criteria, is the one which gives the lowest AIC_C and BIC values. For the choice of one model to be significant one can require differences ΔAIC_C and ΔBIC around 10 (Burnham & Anderson 2010).

4. Case-by-case results

In this section we present the individual analysis for each star. Plots with the radial-velocity data and GLS periodograms are shown in Figs. A.1–A.15 and a summary of the model selection results, for the stars without significant periodogram peaks, is shown in Table 4.

4.1. Candidate planetary signals

HD87838 This star was observed 104 times on 87 different nights. The radial velocities show a dispersion of 2.4 m s^{-1} and a mean uncertainty of 1.3 m s^{-1} . The GLS periodogram shows no significant peaks (Fig. A.1) but the Bayesian analysis finds slight evidence for the presence of one Keplerian signal (Table 4).

The strongest peaks in the periodogram are at 988 d, 68 d and 334 d. The most convincing (highest likelihood) Keplerian fit is a signal with $P = 68.34 \pm 0.46 \text{ d}$, a semi-amplitude $K = 1.9 \pm 0.38 \text{ m s}^{-1}$ and an eccentricity of 0.46 ± 0.16 . If caused by a planet, this signal would correspond to a planet with a minimum mass of $11.14 \pm 2.47 M_{\oplus}$ at an orbital distance of $0.322 \pm 0.001 \text{ AU}$. The phase-folded radial-velocities for this solution are shown in Fig. 2.

Analysing the $\log R'_{\text{HK}}$ and FWHM activity indicators, we do not find strong periodicities close to 68 d (Fig. 3), and therefore it is unlikely that this signal is caused by stellar activity (indeed, the periodogram of the FWHM shows a non-significant peak close to the estimated rotation period). Since the Bayesian

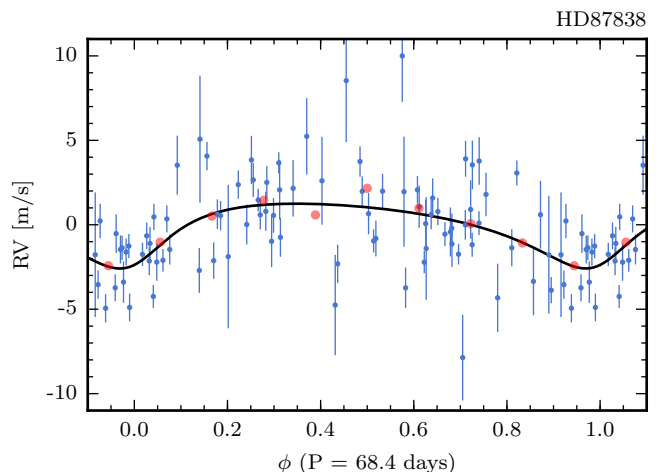


Fig. 2. Phase-folded RV curve for HD87838, with a period of 68.42 d. The blue points are the measured radial-velocities, red circles are binned in phase, with a bin size of 0.1.

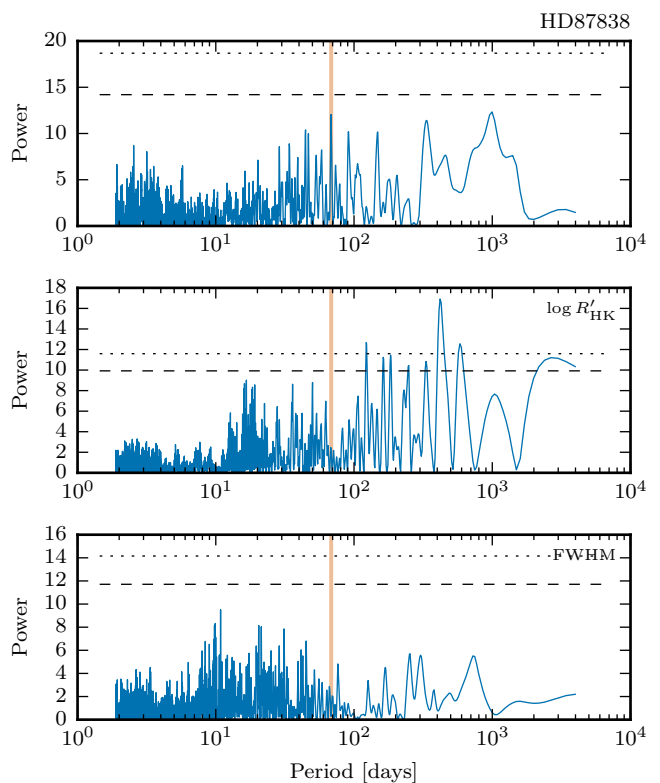


Fig. 3. Periodograms of the radial velocities (top) the $\log R'_{\text{HK}}$ (middle) and the FWHM of the CCF for HD87838. The vertical line shows the orbital period of the candidate planet, at 68.3 d.

analysis only gives marginal evidence for a Keplerian signal (a Bayes factor of 1.75 is “not worth more than a bare mention” in the scale of Kass & Raftery 1995), we consider that this detection is marginal and needs further confirmation. More data would certainly shed light on its true origin, and we will continue to observe this star in the future.

HD175607 This star’s periodogram (Fig. A.2) shows a very significant peak at 29 d, coinciding almost exactly with the estimated rotation period (see Table 1). Some of the longer periods found in the RVs are also present in the $\log R'_{\text{HK}}$ indicator, but no indication of the 29 d period is found in any of the activity proxies. A full analysis of these data is presented in Mortier et al. (2016) where the authors find evidence for (at least) one Neptune-mass planetary companion. In Sect. 6, we consider the detection limits after having removed this orbital solution.

4.2. Signals caused by stellar activity

The effects of stellar activity on radial-velocity observations can be broadly divided in short-term effects, modulated by the stellar rotation, and long-term effects caused by global activity cycles (Baliunas et al. 1995). The activity-induced signals can be diagnosed using activity proxies like line-profile indicators (Queloz et al. 2001; Dumusque et al. 2011a; Boisse et al. 2011) or the $\log R'_{\text{HK}}$ values (e.g. Bonfils et al. 2007). One way to correct the radial velocities for the effects of stellar activity is to assume a linear correlation between, e.g., the $\log R'_{\text{HK}}$ activity index and the activity-related radial-velocity variations and remove this correlation from the RVs (e.g. Melo et al. 2007). Assuming an estimate of the rotation period of the star, one can also subtract sinusoidal functions from the RVs, at the rotation period and its harmonics (e.g. Boisse et al. 2011). The following four stars show evidence for these activity-induced signals.

HD21132 A total of 85 (107 before binning) radial-velocity measurements were obtained for this star, spanning a baseline of over 10 years. The average error bar and dispersion are relatively high, probably due to the high effective temperature (implying a higher oscillation and granulation noise, Dumusque et al. 2011b). All the peaks in the periodogram are below the 1% FAP (Fig. A.3). The model selection analysis nevertheless finds positive evidence for one Keplerian signal, with the best solution having a period of 3712 d and a 4.9 m s^{-1} amplitude.

The very long period of this solution (the timespan of observations is 3935 d) leads us to believe that it is not of planetary origin. In fact, some of peaks at long periods, seen in the periodogram of the RVs, are also found in the periodogram of the $\log R'_{\text{HK}}$. When the RVs are corrected with a linear variation on this indicator, these peaks show a clear decrease in power (Fig. 4). No additional signals were found after applying this correction. We thus conclude that the marginally significant signal found in the data of HD21132 is probably best explained by a long-term magnetic cycle with a period around 10 years.

HD41248 This star was the subject of a recent debate regarding the presence of a planetary system composed of two super-Earths. From an analysis of the first ~ 60 measurements of this dataset, Jenkins et al. (2013b) found evidence for the presence of two planets, at orbital periods of 18.357 d and 25.648 d. Adding about 160 new radial-velocities, Santos et al. (2014) attributed one of the signals (25 d) to activity and could not recover convincing evidence for the second planet. More recently, Jenkins & Tuomi (2014) re-analysed the new data and again found the two planet model to be the most probable. No new measurements were made for this star following the latter two works, but we include it here for completeness.

The period at 25 d is found to be significant, both in the periodogram and from the model selection analysis (with an odds

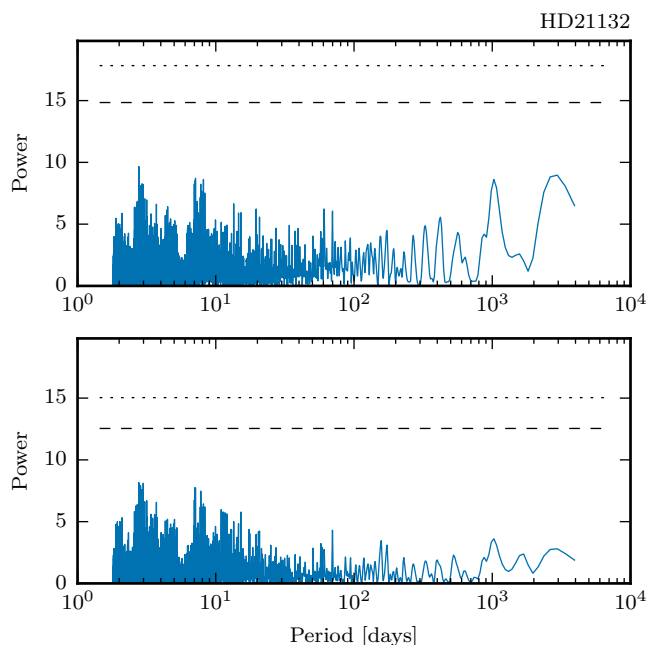


Fig. 4. Periodograms of the radial-velocities of HD21132, before (top) and after (bottom) correcting for a linear variation with $\log R'_{\text{HK}}$.

ratio³ of $\sim 6 \times 10^4$). This would be very strong evidence in favour of (at least one) planetary companion. However, both the FWHM of the HARPS CCF and the $\log R'_{\text{HK}}$ show significant peaks at the same period (Fig. 5). In light of this evidence we must consider this signal to be caused by stellar activity (see also Suárez Mascareño et al. 2015).

The 18 d peak is not recovered clearly in the full dataset. In addition, a convincing detection of this planet presupposes a correction for the activity-induced signal. When attempting to perform this correction, by removing sinusoids at 25 d and its harmonics, we do not find convincing evidence for the 1-planet model. The orbital period of the reported planet, as detected by Jenkins & Tuomi (2014), is also very close to our estimate of the rotation period. It is clear that the currently available data do not allow a firm conclusion on the presence of a planetary system around HD41248.

HD56274 This star was followed closely for over 11 years, with 228 observations in 161 nights. The RVs show a clear long term modulation (Fig. 6), which is also evident from the periodogram (Fig. A.5). This modulation is correlated with the $\log R'_{\text{HK}}$ indicator (Fig. 7) which shows a clear long-term magnetic cycle. The periodogram of the $\log R'_{\text{HK}}$ values suggests a period of over 10 years for this activity cycle.

From the relations of Noyes et al. (1984a) and Mamajek & Hillenbrand (2008), we estimate the rotation period of HD56274 to be around 13 d (see Table 1). A peak at this period appears in the periodogram of the RV data, slightly above the 1% FAP line, but not in the observed values of the activity indicators. Interestingly, when removing a cubic polynomial from the $\log R'_{\text{HK}}$ values (as a correction for the magnetic cycle) a peak at 14.5 d appears in the periodogram of the residuals, although not at a significant level. This suggests that the rotation period of the star

³ The odds ratio cannot be compared to the one found by Jenkins & Tuomi (2014) because we did not use the same model for the RVs.

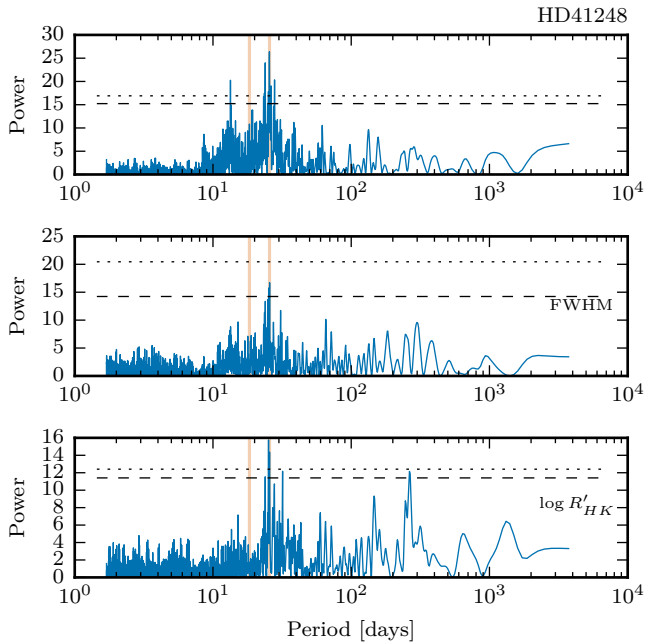


Fig. 5. Periodograms of the radial-velocities, FWHM and $\log R'_{HK}$ for HD41248. The vertical lines show the periods of the planets announced by Jenkins et al. (2013b).

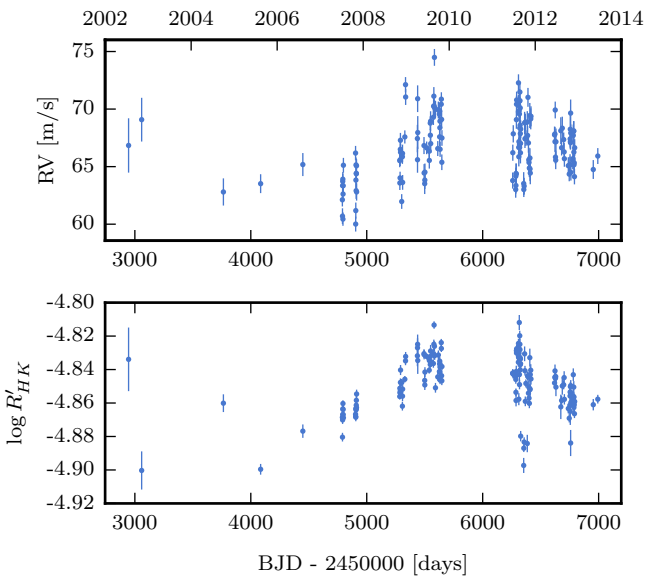


Fig. 6. Time series of the radial velocities (top) and $\log R'_{HK}$ activity index (bottom) for HD56274.

is indeed around 14 d such that this signal is present in both RVs and the $\log R'_{HK}$.

To try to correct the RVs for the long-term activity-induced signal, we removed a linear correlation both with $\log R'_{HK}$ and with FWHM (which also correlates with the RVs). The periodograms of the corrected RVs are shown in Fig. 8. Correcting with $\log R'_{HK}$ removes most of the long period peaks but leaves in the periodogram the peaks associated with one year aliases. The cause for these peaks is probably the same instrumental effect identified in the case of HD88725 (see Sect. 4.3). No other significant signals can be found in the residual data. The cor-

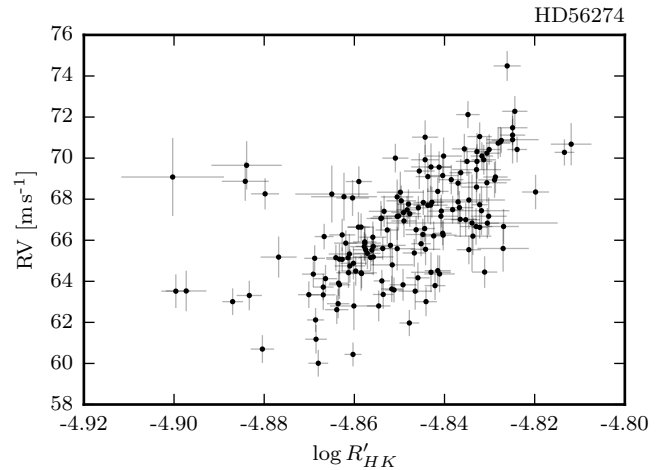


Fig. 7. Radial-velocity versus the $\log R'_{HK}$ activity indicator for HD56274. We estimate the posterior distribution for Spearman's rank correlation coefficient using an MCMC. The posterior has a mean value of 0.62 and a 95% credible interval [0.52, 0.71] for these data, suggesting a tight correlation, likely caused by a long-term activity cycle.

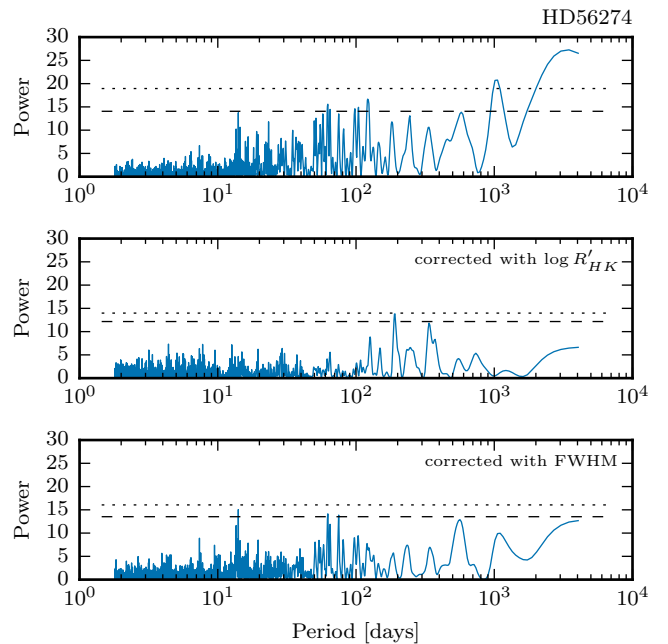


Fig. 8. The top panel shows the GLS periodogram of the observed radial-velocities of HD56274. The middle and bottom panels show the periodograms after correcting the RVs from linear correlations with the $\log R'_{HK}$ activity indicator and the FWHM, respectively.

rection with the FWHM reveals a significant peak at 14 d (close to the estimated rotation period) and two peaks at 62 d and 74 d. With this second correction, however, the long-term periodicities are not completely removed. We conclude that with the available data, and after correcting for the long-term magnetic cycle, it is not possible to assert the presence of planets orbiting this star.

HD114076 The rotation period for this star is estimated to be between 41 and 43 d, depending on the calibration (Table 1). The periodogram (Fig. 9 top panel, and Fig. A.6) shows a cluster of

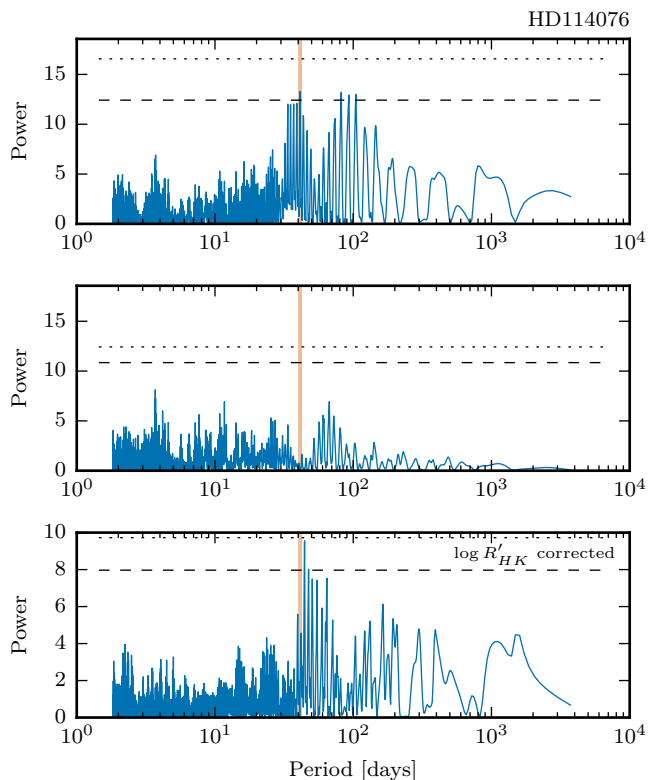


Fig. 9. Periodogram for HD114076 before (top) and after (middle) fitting and removing a sine function to correct for activity-induced variations. The vertical dashed line marks the best fit period of 41.27 d. The bottom plot shows the periodogram of the $\log R'_{HK}$ index after removing a quadratic polynomial from the observed values.

peaks around 40 d and also around 80 d. The strongest peak is at 41.3 d and very close to the 1% FAP.

To correct the RVs from what we believe is an activity-induced signal, a sine function was fitted and subtracted from the data. The best fit period was 41.27 d, and the periodogram of the residuals, shown in Fig. 9 (bottom panel), does not present additional significant signals.

To confirm that this signal is caused by the rotation of the star, we analysed the activity indicators. In particular, the $\log R'_{HK}$ shows a clear long-term trend, which might be caused by a magnetic cycle. We tried to remove the long-term variations by fitting both quadratic and cubic polynomials to the $\log R'_{HK}$ observations. The residuals of both fits show a clear periodic signal at 44.4 d which helps to corroborate the activity-induced nature of the 41 d signal in the RVs.

4.3. Sampling and instrumental effects

One additional obstacle in the detection of periodic RV variations due to planets is the presence of spurious signals and periodicities caused by the discrete time sampling of the observations or by instrumental effects. These can originate, amongst other effects, from Earth's rotation and orbital motion. The following stars show evidence of contaminations of this kind.

HD22879 Although the periodogram of this star (Fig. A.7) does not show significant peaks, the Bayesian analysis finds evidence for the presence of one Keplerian signal with a period of

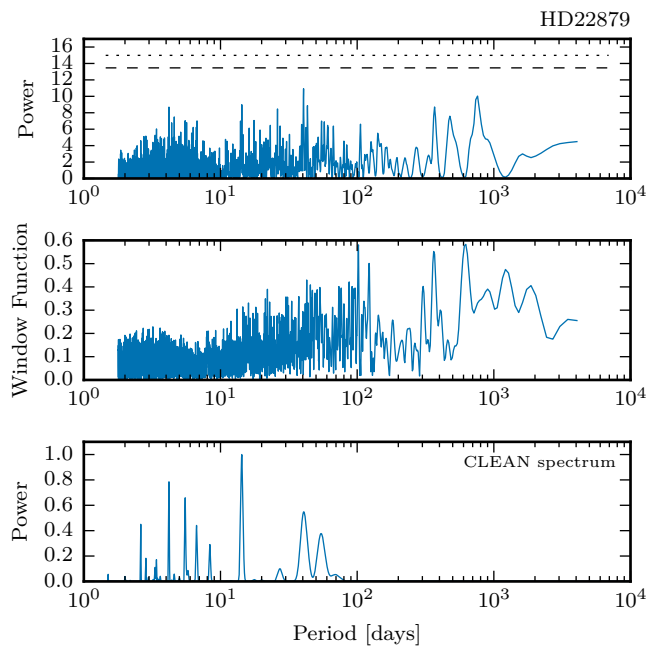


Fig. 10. Periodogram, window function and CLEAN spectrum for the radial-velocities of HD22879.

~ 770 d and an eccentricity of 0.7. This corresponds to the second highest peak in the periodogram.

We find that this signal can, however, be caused by the time sampling of the observations. In the top and middle panels of Fig. 10, we show the periodogram together with the window function of the observations. The window function is calculated as the Fourier transform of the observation times (Roberts et al. 1987; Dawson & Fabrycky 2010) and provides information on the power that is introduced in the periodogram due to the sampling.

The CLEAN algorithm, introduced for frequency analysis by Roberts et al. (1987), is a well-known method to deconvolve the observed spectrum and the window function, thereby reducing the artifacts introduced by the sampling. Applying the CLEAN algorithm to the RV measurements of HD22879, results in the spectrum shown in the bottom panel of Fig. 10. The highest peak is at 14 d, which is close to the estimated stellar rotation period. It is not clear if this power is activity-induced, since the activity indicators do not show any clear signal at this period (nor any long-term drifts).

We conclude that the Keplerian signal found at 770 d is best explained as originating from the time sampling. It is worth mentioning here that the Bayesian analysis is vulnerable to this kind of signals because it does not take into consideration, at any stage, the information present in the window function.

HD79601 The periodogram of the radial-velocities of this star shows one significant peak at ~ 550 d (Fig. A.8). A Keplerian fit at this period results in a solution with $P = 532.85 \pm 9.63$ d, a semi-amplitude of 1.92 ± 0.28 m s $^{-1}$ and an eccentricity of 0.55 ± 0.18 . A planet with these parameters would have a mass of $20.4 \pm 4.16 M_{\oplus}$. The phase-folded radial-velocities for this solution (Fig. 11) show that the phase coverage is not ideal. The residuals from this fit do not show any significant periodogram peaks or evidence for additional signals.

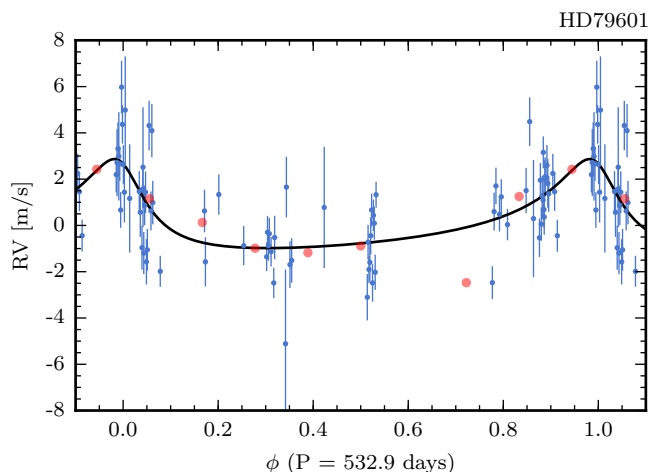


Fig. 11. Phase folded radial-velocity measurements (blue) of HD79601 with a period of 532.9 days. The red circles are binned in phase, with a bin size of 0.1, and the black line shows the best fit Keplerian function.

The lack of a good phase coverage of the orbital solution, puts the planetary hypothesis in question. From Fig. A.8 it is clear that the measurements were obtained in several series, separated by large time gaps. Looking only at the observations after BJD= 2454500, the data show hints for a linear drift. When a linear drift is removed from this subset of the data (and also when a quadratic drift is removed from the full dataset), the peak at 550 d vanishes and no other significant peaks remain in the periodogram of the residuals. At this point, our data do not allow us to reach any firm conclusions about the nature of the signal observed for HD79601.

HD88725 The radial velocities of this star show a significant periodicity at 368.3 d (Fig. A.9). Because this period is close to one year, we measured the correlation between the radial-velocity and the barycentric Earth radial velocity (BERV). The posterior distribution for Spearman’s rank correlation coefficient (which was sampled using MCMC; see Figueira et al., submitted) has a mean of -0.29 and a 95% credible interval (the highest posterior density interval) is $[-0.46, -0.13]$. This anti-correlation suggests that the signal detected in the RVs might be induced by the orbit of the Earth around the Sun.

Dumusque et al. (2015) recently described the cause for signals of this type to show up in HARPS radial-velocities, and suggested a method to correct for this effect: the spectral lines that cross the so-called block stitchings in the HARPS CCD can be identified in the correlation mask used to derive the RVs. We created two different correlation masks, one with only the lines falling close to the block stitchings, and one without those lines.

For the case of HD88725, the periodograms of the RVs derived with the original mask and both custom masks are shown in Fig. 12. The spectral lines that cross the block stitching are the origin of the peak at one year (middle panel) and when those lines are removed from the correlation mask, the peak vanishes from the periodogram (bottom panel). After the RVs are corrected, the periodogram does not show significant peaks and we do not find evidence for the presence of Keplerian signals.

HD111777 In Fig. 13, the periodogram of the 79 measurements of this star is plotted together with the spectral window function

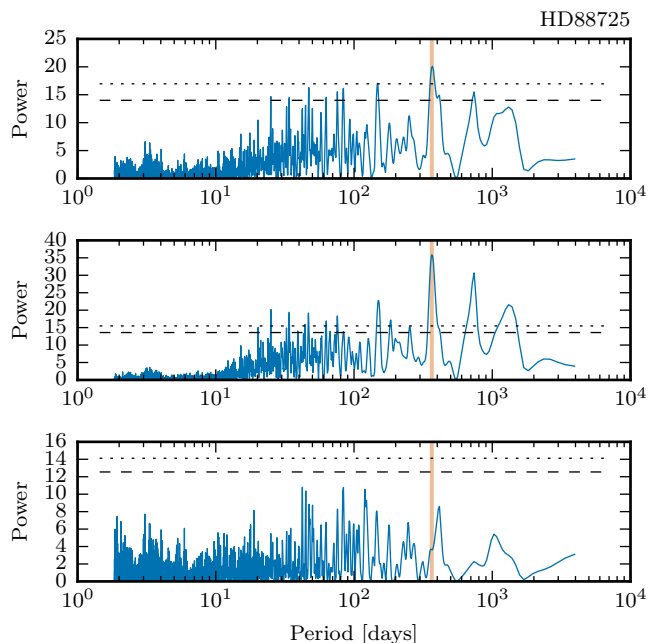


Fig. 12. Periodograms of the original radial-velocities of HD88725 (top panel), the radial-velocities derived using a correlation mask that contains only the spectral lines crossing the CCD block stitchings (middle panel), and the radial-velocities derived using a correlation mask without those lines (bottom panel). The vertical line shows the orbital period of the Earth.

(see also Fig. A.10). Although there are significant peaks in the periodogram, it becomes impossible to identify clear peaks produced by physical signals, because of the confusion introduced by the sampling. This does not mean that a long period signal is not present, only that the highest peak in the periodogram can show up in a different location due to the sampling.

Since the window function shows only excess power for long periods, and not distinct peaks, the CLEAN algorithm does not provide a good correction in this case. The large gap without observations is what causes these issues. After considering only the better-sampled subset of the data (after BJD=2456000), we do not find any significant signals. Also, after removing a linear trend⁴ from the full dataset, the periodogram of the residuals does not show any significant peaks.

The periodograms of the activity indicators do not help in corroborating the presence of a planetary signal: the FWHM shows a non-significant periodicity close to 730 days but the highest peak in the periodogram of the $\log R'_{\text{HK}}$ is at 16 days. We conclude, for the case of HD111777, that we are currently not able to assess the presence of a signal that might originate from a long-period planetary companion.

HD224817 The periodogram of the RVs of this star (Fig. A.11) does not show peaks above the 1% FAP line, but the model selection analysis finds the model with one Keplerian to be the most probable. In the scale of Kass & Raftery (1995), an odds ratio of 1.25 (Table 4) is “not worth more than a bare mention”.

The highest peak in the periodogram is at ~ 245 d – the best fit Keplerian also converges to this solution – but this period is probably caused by the deformation of the spectral lines that

⁴ For consistency, we checked that the evidence of the constant model is higher than that of a model with an added linear drift parameter.

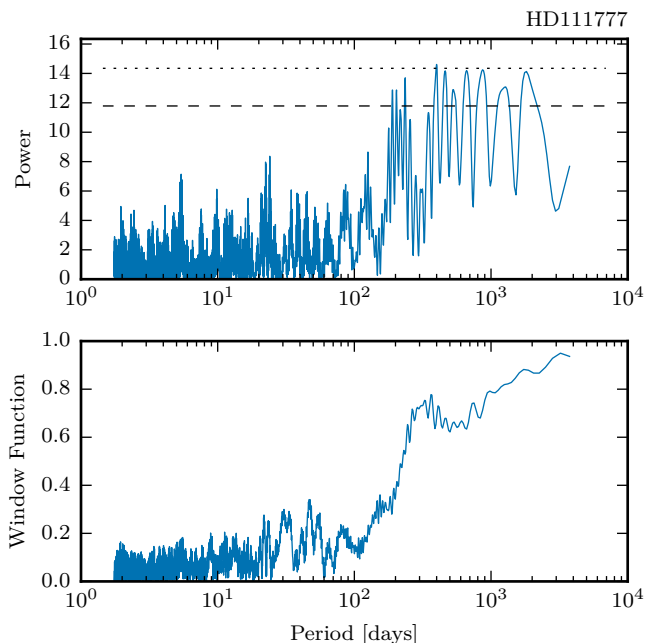


Fig. 13. Periodogram and window function for HD111777.

cross the block stitchings of the HARPS CCD, as for the case of HD88725. We noticed this when fitting and removing from the RVs a sinusoid with a period of 1 year decreased the power of the 245 d peak.

To further check that the signal is indeed caused by the instrument, we created different correlation masks both with and without the lines falling close to the block stitchings (Dumusque et al. 2015). The periodograms for the original RVs and those from the two custom masks are shown in Fig. 14. When the spectral lines that cross the block stitchings are removed from the correlation mask, the 245 d peak vanishes from the periodogram (bottom panel). The periodogram of the corrected RVs does not show significant peaks and we do not find evidence for the presence of Keplerian signals.

The second highest peak in the periodogram of the original radial velocities, around 10 d, is not far from the estimated rotation period of the star (Table 1). A clear (though not significant) peak at this period is present in the periodogram of the FWHM indicator. We conclude that the data available for HD224817 does not suggest the presence of any planetary companions.

4.4. Stars without identified signals

HD31128 This star was followed very closely with a total of 215 radial-velocity measurements on 169 different nights. These numbers already take into account an outlier observation at BJD = 2455304.48 which was removed prior to the analysis. This observation has a very low CCF contrast value, making us suspect of some instrumental or observational error at this date.

The RV data show a high dispersion though the average uncertainty is also above 3 m s^{-1} . These can be explained by the high effective temperature and very low metallicity of this star, which hinder the precise calculation of the radial-velocity with the CCF technique (low metallicity stars within this temperature range have shallower lines, making the determination of precise RVs more difficult, while the higher temperature intro-

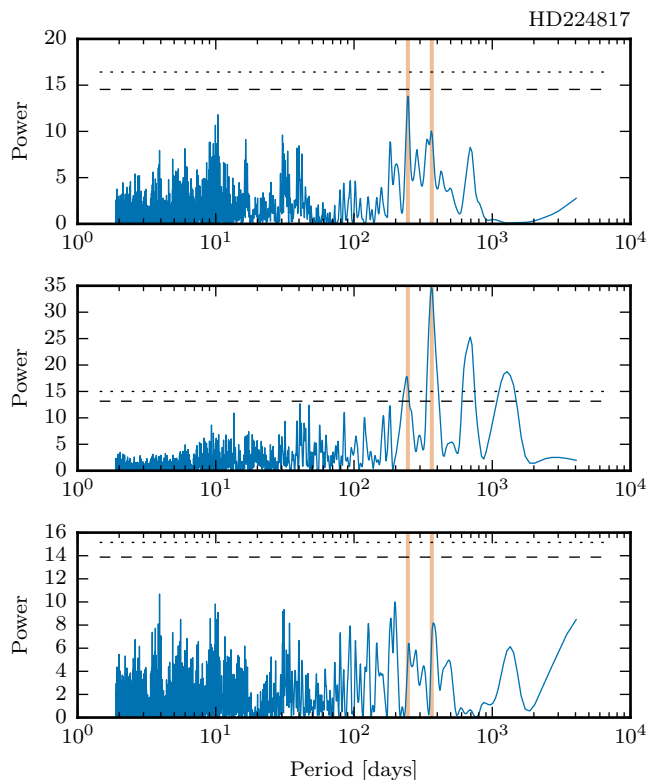


Fig. 14. Periodograms of the original radial velocities of HD224817 (top panel), the RVs derived with a correlation mask that contains only the spectral lines crossing the CCD block stitchings (middle panel), and those derived using a correlation mask without those lines (bottom panel). The vertical lines show the period of the highest peak in the top periodogram and the orbital period of the Earth.

duces higher oscillation and granulation noise levels; Dumusque et al. 2011b)

Despite the large number of measurements, none of the periodogram peaks are significant (Fig. A.12). According to the model selection analysis, there is no evidence for planetary companions orbiting this star. The constant model is preferred relative to the 1-planet model according to the value of the evidence (with an odds ratio of 2.5) and the BIC (with ΔBIC of 5.4). However, the AIC_C selects instead the 2-planet model but, in light of our general results (see Sect. 5), we tend to trust the Bayesian criteria.

HD119173 This star was observed on 98 different nights (totalling 128 measurements) which cover a total timespan of 8.1 years. No significant periodogram peaks were found (Fig. A.13), and in the model selection analysis the constant model is preferred over the 1-planet model (with odds ratio $O_{01} \sim 4.5$ and $\Delta\text{BIC} = 8.7$). We conclude that there is no evidence for the presence of planetary signals in these data.

HD119949 The periodogram of the 81 measurements, shown in Fig. A.14, does not present any significant peaks. The Bayesian search for Keplerian signals reaches the same conclusions (odds ratio $O_{01} \sim 4$). The AIC_C again selects a more complex 1-planet model with a non-significant ΔAIC_C . We report no clear evidence for planetary companions.

HD126793 A total of 96 measurements on 79 different nights were obtained. The periodogram (Fig. A.15) does not show any significant peaks and, in this case as well, the model comparison does not find evidence for Keplerian signals in the data. For these data, all model selection criteria select the constant model as the most probable with $O_{01} \sim 4$, $\Delta AIC_C = 1.1$, $\Delta BIC = 11.5$.

5. Comparison of model selection criteria

For the maximum-likelihood solutions, the AIC_C and BIC can be calculated using the number of free parameters in a given model. These are sometimes used as model selection criteria, and are much easier to calculate than the value of the evidence. In Table 4 we show the AIC_C and BIC values for each star and model, using the maximum-likelihood obtained from all MULTINEST samples. We highlight in bold the best model according to each criteria.

As general trends in our results we can note that the AIC_C tends to choose a model with a higher number of Keplerian signals. The BIC is found to be more conservative and tends to agree with the model with the highest evidence. These results suggest that the BIC can be used as a viable approximation to the evidence, given that the (global) maximum of the likelihood function can be found.

6. Detection Limits

Many of the stars we analysed in Sect 4 do not contain significant periodic signals or show signals originating from activity and sampling contaminations. In this section, we derive upper limits to the planetary signals that can be present and yet still undetectable in these data. For a given star we determine which planet, as a function of its mass and orbital period, can already be ruled out with our observations.

The detection limits are calculated with a standard procedure: injecting trial circular orbits into the observed data (Cumming et al. 1999; Endl et al. 2001; Zechmeister et al. 2009; Dumusque et al. 2011c; Mayor et al. 2011; Mortier et al. 2012). We explore all periods in the range from 1 d to 500 d and semi-amplitudes from 0 to 10 m s^{-1} (using a binary search). For 10 linearly-spaced phases, we compare the periodogram power of the injected period with the FAP level of that period in the original dataset. If, for all phases, the former is higher we consider the planet to be detected. We convert the semi-amplitude to planetary mass using the stellar masses listed in Table 1.

It is important to note that this method assumes the original dataset (in which mock planets are injected) to contain only non-correlated noise. For the stars analysed in Sect. 4.4, this assumption is valid. For the stars analysed in Sect. 4.1, we subtracted the putative orbital solution from the data before calculating the detection limits. Since correcting for activity-induced signals and artifacts originating from the sampling is much more prone to error, for the stars discussed in Sects. 4.2 and 4.3, we assume that the observed radial-velocities contain only noise. Therefore, for this last group of stars, the detection limits estimates can be taken as conservative.

The detection limits for all 15 stars are shown in Fig. 15. The plots show minimum mass, in Earth masses, against orbital period. The black curves correspond to the 99% detection limits and the blue dashed curves indicate circular planetary signals with RV semi-amplitudes of 1, 3 and 5 m s^{-1} . The red dotted regions correspond to planets with $P < 50 \text{ d}$, and masses in the ranges $M = 10 - 30 M_{\oplus}$ and $M = 30 - 100 M_{\oplus}$. These can be

compared to the same regions considered in (Mayor et al. 2011) for the calculation of the planet occurrence rate.

Almost uniformly in this sample, we are sensitive to planets more massive than $10 M_{\oplus}$ up to orbital periods of 50 days. For shorter period planets, with $P \sim 10$ days and smaller, the current data would already allow for the detection of planets with just a few Earth masses.

7. Discussion and conclusions

From over 100 targets in our metal-poor large program, we selected those which were observed on more than 75 nights. A homogeneous analysis of the radial-velocity observations was carried out by comparing models with a varying number of Keplerian signals. We used the nested sampling algorithm to estimate the evidence of a given model and compared the results with the posterior distribution of the number of Keplerians n . We also calculate the AIC_C and BIC and analyse the periodograms of the radial velocities and activity indicators.

We find, in some cases, a disagreement between the evidence results and the presence of significant periodogram peaks. The Bayesian analysis was able to identify a few Keplerian signals which are not significant in the periodograms. Nevertheless, the values of the odds ratios indicate that these detections are not very significant. The results obtained with MULTINEST almost always⁵ agree with the posterior distribution $p(n|d)$, which is reassuring but not surprising given that the same priors and likelihood were used in both algorithms.

Signals induced by stellar activity were detected for HD21132, HD56274 and HD114076, besides the known case of HD41248. After attempting to correct for these signals, we were not able to recover any additional signs of planetary companions.

For HD79601, HD22879 and HD111777, the time sampling of the observations induces spurious signals in the radial-velocities, hindering the detection of planetary signals. We also identified a clear 1 year periodicity and its harmonics, caused by instrumental effects, on the radial velocities of HD88725 and HD224817. These instrument-induced RV variations are not expected to be present in all stars since each star may have different values of the BERV and different spectral lines crossing the CCD block stitchings (see Dumusque et al. 2015).

HD87838 shows an interesting signal around 68 d, which can be fitted with a slightly eccentric Keplerian. The model selection does not provide strong evidence for the presence of this planet but we hope to obtain more data to assert its nature.

It is important to note that the value of the evidence (and our estimate) is sensitive to the priors on the parameters of a given model. This is not necessarily a limitation, meaning only that care should be taken when choosing the priors and that they should be stated clearly in any analysis.

As an example of these points, we re-analysed the data of HD87838 with $n = 1$, considering the prior for the orbital period to be uniform between 65 d and 75 d⁶. The resulting value for the evidence was found to be -209.5 , in contrast to the value determined previously, of -213.9 (Table 4). This corresponds to an odds ratio of ~ 156 against the constant model, which would imply “very strong” evidence for a Keplerian signal and a confident planet detection.

⁵ The exceptions are the 2-planet models for HD87838 and HD224817. This can be due to poorer sampling by one of the algorithms or incomplete convergence.

⁶ The example is contrived but might shed light on why one should not adjust the priors after having looked at the data (or the periodogram, for that matter).

Table 4. Model selection results for the stars without significant periodogram peaks. For each star and each model we show the logarithm of the evidence, the odds ratio with respect to the constant model, the (normalised) value of the posterior distribution $p(n|d)$ and the AIC_C and BIC for the maximum-likelihood solution.

	$\ln E$	O_{i0}	$p(n d)^{(1)}$	$AIC_C^{(2)}$	BIC ²
HD21132					
constant	-229.5	1	■	452.1	456.9
1 keplerian	-227.7	6.13	■■■■	443.7	459.3
2 keplerians	-229.0	1.54	■■■	438.5	463.5
HD22879					
constant	-164.8	1	■	322.2	326.8
1 keplerian	-162.8	7.87	■■■■	300.8	315.9
2 keplerians	-164.3	1.76	■■■	303.3	327.2
HD31128					
constant	-473.9	1	■■■■	940.7	946.9
1 keplerian	-474.9	0.40	■■■	931.0	952.3
2 keplerians	-475.7	0.17	■	919.1	954.8
HD87838					
constant	-214.5	1	■■■	421.4	426.2
1 keplerian	-213.9	1.75	■■■■	410.8	426.6
2 keplerians	-215.1	0.56	■■■	411.2	436.6
HD119173					
constant	-202.0	1	■■■■	397.1	402.1
1 keplerian	-203.5	0.23	■	393.9	410.8
2 keplerians	-205.8	0.02	■	402.6	429.9
HD119949					
constant	-188.5	1	■■■■	370.1	374.8
1 keplerian	-189.9	0.25	■	366.8	382.0
2 keplerians	-191.8	0.03	■	377.6	401.7
HD126793					
constant	-174.1	1	■■■■	341.0	345.6
1 keplerian	-175.6	0.23	■	342.1	357.1
2 keplerians	-176.8	0.07	■	350.3	373.9
HD224817					
constant	-218.1	1	■■■	428.8	433.9
1 keplerian	-217.8	1.25	■■■■	418.3	435.3
2 keplerians	-218.9	0.40	■■■	416.2	443.9

Notes. ⁽¹⁾ The bars represent the posterior distribution for the number of keplerians in the model. For each star, this posterior is normalized to the value in the most probable bin. ⁽²⁾ Calculated using maximum likelihood value from all MultiNest samples and the number of free parameters for each model.

We performed a sensitivity analysis of our results, namely by considering different priors for the orbital periods and semi-amplitudes. Even if, in some cases, a different model would be preferred (that is, yield a higher evidence), the absolute value of the Bayes factors did not change considerably. This means that our level of confidence in the presence or not of a planetary signal does not depend severely on the parameter priors.

Even though our working sample is small, it already allows for an analysis of the frequency of planets around these stars. We do not attempt to provide constraints on the planet frequency as a function of stellar metallicity, since our sample does not span completely the metallicity space (Fig. 1).

The probability of obtaining k detections in a sample of size N is given by the binomial distribution, assuming a planet fre-

quency f_p

$$p(k|N, f_p) = \frac{N!}{k!(N-k)!} f_p^k (1-f_p)^{N-k} \quad (5)$$

This equation can be thought of as a function of f_p for given values of k and N , therefore representing a (un-normalised) posterior distribution for f_p . The number of planets detected in a given sample places a constraint on the probable values of the planet frequency, which can be expressed by the mode and the range that covers, e.g., 68% of the distribution.

Considering the detection of the planet orbiting HD175607, in a sample of 15 stars, this procedure gives a constraint of $f_p = 6.67\%_{-5.58\%}^{+4.16\%}$. Taking into account also the unconfirmed planet around HD87838, one obtains $f_p = 13.33\%_{-8.84\%}^{+5.80\%}$. This last result is in agreement with that of Mayor et al. (2011), who

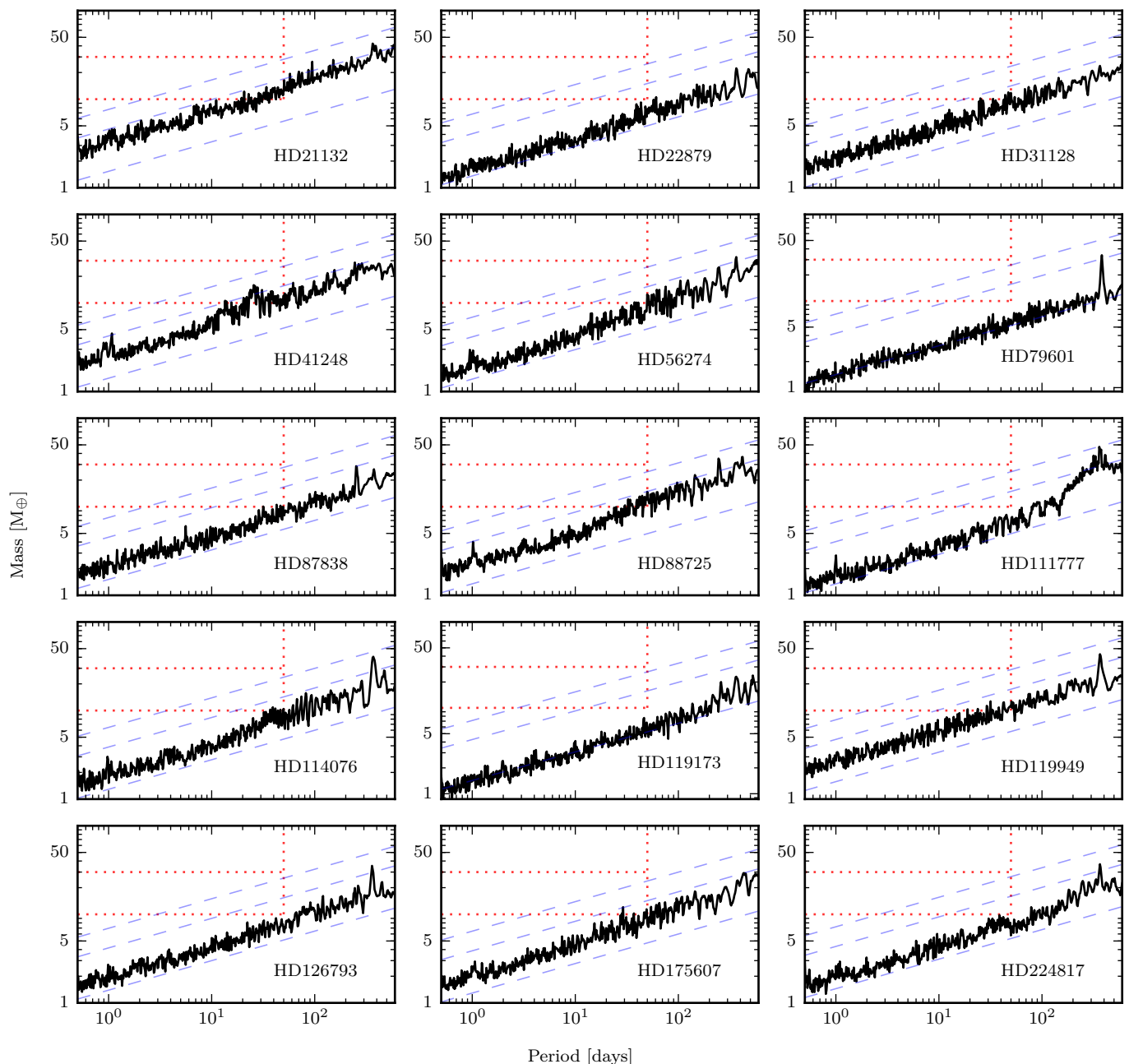


Fig. 15. Detection limits for the 15 stars studied in this work. The plots show planetary mass against orbital period. The thick black line shows the 99% detection limits, estimated by injecting trial circular orbits. The dashed blue lines represent circular planetary signals with RV semi-amplitudes of 1, 3 and 5 m s^{-1} (from bottom to top in each panel). The regions delimited by the red dotted lines correspond to periods lower than 50 d, and masses in the ranges $M = 10 - 30 M_{\oplus}$ and $M = 30 - 100 M_{\oplus}$.

found $12.27 \pm 2.45\%$ for the combined occurrence rate of planets with orbital periods smaller than 50 days and masses in the range $M = 10 - 100 M_{\oplus}$. We nevertheless stress that our constraints on the planet occurrence rate are preliminary, since they are based on a small sample and subject to selection biases.

Recent studies have identified correlations between the properties of the planetary system and the metallicity of the star. Lower metallicity stars have been found to host longer period planets (Beugé & Nesvorný 2013; Adibekyan et al. 2013) or lower eccentricity orbits (Dawson & Murray-Clay 2013). These results, together with the detection limits calculated in Sect 6, might explain why few planets have been detected so far in our sample. The search for low-mass planets around metal-poor stars

requires not only high-precision radial velocities but also a very long baseline of observations.

Our results show that the detection of small planets in these data is hindered by time sampling issues and activity-induced signals. Careful planning of the observational strategy and detailed analyses of the aliasing structures are necessary to mitigate some of these problems and we must seek ways to make use of all the information contained in the RVs and in all the activity indicators, in an optimal and physically-meaningful way.

The analysis of the full sample of 109 metal-poor stars is ongoing and we expect to provide constraints on the frequency of planets orbiting these stars when the observations of the Large Program are finished.

Acknowledgements. This work was supported by Fundação para a Ciência e a Tecnologia (FCT) through the research grant UID/FIS/04434/2013. We also acknowledge the support from FCT in the form of grant reference PTDC/FIS-AST/1526/2014. JPF acknowledges the support from FCT through the grant reference SFRH/BD/93848/2013 and thanks Brendon Brewer for his assistance with the diffusive nested sampling code. PF and NCS acknowledge support by FCT through Investigador FCT contracts of reference IF/01037/2013 and IF/00169/2012, respectively, and POPH/FSE (EC) by FEDER funding through the program “Programa Operacional de Factores de Competitividade - COMPETE”. PF further acknowledges support from FCT in the form of an exploratory project of reference IF/01037/2013CP1191/CT0001. AM received funding from the European Union Seventh Framework Program (FP7/2007-2013) under grant agreement number 313014 (ETA-EARTH). AS is supported by the European Union under a Marie Curie Intra-European Fellowship for Career Development with reference FP7-PEOPLE-2013-IEF, number 627202.

References

- Adibekyan, V., Santos, N. C., Figueira, P., et al. 2015, *A&A*, 581, L2
- Adibekyan, V. Z., Delgado Mena, E., Sousa, S. G., et al. 2012, *A&A*, 547, A36
- Adibekyan, V. Z., Figueira, P., Santos, N. C., et al. 2013, *A&A*, 560, A51
- Baliunas, S. L., Donahue, R. A., Soon, W. H., et al. 1995, *ApJ*, 438, 269
- Baranne, A., Queloz, D., Mayor, M., et al. 1996, *A&AS*, 119, 373
- Beaugé, C. & Nesvorný, D. 2013, *ApJ*, 763, 12
- Boisse, I., Bouchy, F., Hébrard, G., et al. 2011, *A&A*, 528, A4
- Bonfils, X., Mayor, M., Delfosse, X., et al. 2007, *A&A*, 474, 293
- Brewer, B. J. & Donovan, C. P. 2015, *MNRAS*, 448, 3206
- Brewer, B. J., Pártay, L. B., & Csányi, G. 2011, *Stat. Comput.*, 21, 649
- Buchhave, L. A. & Latham, D. W. 2015, *ApJ*, 808, 187
- Buchhave, L. A., Latham, D. W., Johansen, A., et al. 2012, *Nature*
- Burnham, K. P. & Anderson, D. R. 2010, *Model Selection and Multimodel Inference*, 2nd edn. (Springer)
- Cumming, A., Marcy, G. W., & Butler, R. P. 1999, *ApJ*, 526, 890
- Dawson, R. I., Chiang, E., & Lee, E. J. 2015, *MNRAS*, 453, 1471
- Dawson, R. I. & Fabrycky, D. C. 2010, *ApJ*, 722, 937
- Dawson, R. I. & Murray-Clay, R. A. 2013, *ApJ*, 767, L24
- Dumusque, X., Lovis, C., Ségransan, D., et al. 2011a, *A&A*, 535, A55
- Dumusque, X., Pepe, F., Lovis, C., & Latham, D. W. 2015, *ApJ*, 808, 171
- Dumusque, X., Pepe, F., Lovis, C., et al. 2012, *Nature*, 491, 207
- Dumusque, X., Santos, N. C., Udry, S., Lovis, C., & Bonfils, X. 2011b, *A&A*, 527, A82
- Dumusque, X., Udry, S., Lovis, C., Santos, N. C., & Monteiro, M. J. P. F. G. 2011c, *A&A*, 525, A140
- Endl, M., Kürster, M., Els, S., Hatzes, A. P., & Cochran, W. D. 2001, *A&A*, 374, 675
- Feroz, F., Balan, S. T., & Hobson, M. P. 2011a, *MNRAS*, 416, L104
- Feroz, F., Balan, S. T., & Hobson, M. P. 2011b, *MNRAS*, 415, 3462
- Feroz, F. & Hobson, M. P. 2013, *ArXiv Prepr. ArXiv13076984*
- Feroz, F., Hobson, M. P., & Bridges, M. 2009, *MNRAS*, 398, 1601
- Feroz, F., Hobson, M. P., Cameron, E., & Pettitt, A. N. 2013, *ArXiv Prepr. ArXiv13062144*
- Fischer, D. A. & Valenti, J. 2005, *ApJ*, 622, 1102
- Gonzalez, G. 1997, *MNRAS*, 285, 403
- Gregory, P. C. 2007, *MNRAS*, 374, 1321
- Gregory, P. C. 2010, *Bayesian logical data analysis for the physical sciences* (Cambridge: Cambridge University Press)
- Grunblatt, S. K., Howard, A. W., & Haywood, R. D. 2015, *ApJ*, 808, 127
- Guillot, T., Santos, N. C., Pont, F., et al. 2006, *A&A*, 453, L21
- Hatzes, A. P. 2014, *A&A*, 568, A84
- Ida, S. & Lin, D. N. C. 2004, *ApJ*, 616, 567
- Jenkins, J. S., Jones, H. R. A., Tuomi, M., et al. 2013a, *ApJ*, 766, 67
- Jenkins, J. S. & Tuomi, M. 2014, *ApJ*, 794, 110
- Jenkins, J. S., Tuomi, M., Brasser, R., Ivanyuk, O., & Murgas, F. 2013b, *ApJ*, 771, 41
- Kass, R. E. & Raftery, A. E. 1995, *J. Am. Stat. Assoc.*, 90, 773
- Kipping, D. M. 2013, *MNRAS*, 434, L51
- Lovis, C., Dumusque, X., Santos, N. C., et al. 2011, *ArXiv11075325 Astro-Ph*
- Mamajek, E. E. & Hillenbrand, L. A. 2008, *ApJ*, 687, 1264
- Mayor, M., Marmier, M., Lovis, C., et al. 2011, *ArXiv Prepr. ArXiv11092497*
- Melo, C., Santos, N. C., Gieren, W., et al. 2007, *A&A*, 467, 721
- Mordasini, C., Alibert, Y., Benz, W., & Naef, D. 2009, *A&A*, 501, 1161
- Mordasini, C., Mollière, P., Dittkrist, K.-M., Jin, S., & Alibert, Y. 2015, *Int. J. Astrobiol.*, 14, 201
- Mortier, A., Faria, J. P., Santos, N. C., et al. 2016, *A&A*, 585, A135
- Mortier, A., Santos, N. C., Sousa, S., et al. 2013, *A&A*, 551, A112
- Mortier, A., Santos, N. C., Sozzetti, A., et al. 2012, *A&A*, 543, A45
- Mukherjee, P., Parkinson, D., & Liddle, A. R. 2006, *ApJ*, 638, L51
- Murdoch, K. A., Hearnshaw, J. B., & Clark, M. 1993, *ApJ*, 413, 349
- Naef, D., Mayor, M., Benz, W., et al. 2007, *A&A*, 470, 721
- Neves, V., Bonfils, X., Santos, N. C., et al. 2013, *A&A*, 551, A36
- Noyes, R. W., Hartmann, L. W., Baliunas, S. L., Duncan, D. K., & Vaughan, A. H. 1984a, *ApJ*, 279, 763
- Noyes, R. W., Weiss, N. O., & Vaughan, A. H. 1984b, *ApJ*, 287, 769
- Pepe, F., Mayor, M., Galland, F., et al. 2002, *A&A*, 388, 632
- Perryman, M. A. C. 2014, *The Exoplanet Handbook*, 1st edn. (Cambridge: Cambridge University Press)
- Queloz, D., Henry, G. W., Sivan, J. P., et al. 2001, *A&A*, 379, 279
- Roberts, D. H., Lehar, J., & Dreher, J. W. 1987, *AJ*, 93, 968
- Robertson, P. & Mahadevan, S. 2014, *ApJ*, 793, L24
- Santos, N. C., Adibekyan, V., Mordasini, C., et al. 2015, *A&A*, 580, L13
- Santos, N. C., Israelian, G., & Mayor, M. 2004, *A&A*, 415, 1153
- Santos, N. C., Mayor, M., Bonfils, X., et al. 2011, *A&A*, 526, A112
- Santos, N. C., Mayor, M., Bouchy, F., et al. 2007, *A&A*, 474, 647
- Santos, N. C., Mayor, M., Naef, D., et al. 2000, *A&A*, 361, 265
- Santos, N. C., Mortier, A., Faria, J. P., et al. 2014, *A&A*, 566, A35
- Schneider, J., Dedieu, C., Le Sidaner, P., Savalle, R., & Zolotukhin, I. 2011, *A&A*, 532, A79
- Sivia, D. S. & Skilling, J. 2006, *Data Analysis: A Bayesian Tutorial* (Oxford: Oxford University Press)
- Skilling, J. 2004, in *Bayesian Inference and Maximum Entropy Methods in Science and Engineering*, Vol. 735, Garching (Germany), 395–405
- Sousa, S. G., Santos, N. C., Israelian, G., et al. 2011a, *A&A*, 526, A99
- Sousa, S. G., Santos, N. C., Israelian, G., Mayor, M., & Udry, S. 2011b, *A&A*, 533, A141
- Sousa, S. G., Santos, N. C., Mayor, M., et al. 2008, *A&A*, 487, 373
- Sozzetti, A., Torres, G., Latham, D. W., et al. 2009, *ApJ*, 697, 544
- Suárez Mascareño, A., Rebolo, R., González Hernández, J. I., & Esposito, M. 2015, *MNRAS*, 452, 2745
- Tinney, C. G., Butler, R. P., Marcy, G. W., et al. 2002, *ApJ*, 571, 528
- Udry, S., Mayor, M., Benz, W., et al. 2006, *A&A*, 447, 361
- Udry, S. & Santos, N. C. 2007, *ARA&A*, 45, 397
- Wang, J. & Fischer, D. A. 2014, *AJ*, 149, 14
- Zechmeister, M. & Kürster, M. 2009, *A&A*, 496, 577
- Zechmeister, M., Kürster, M., & Endl, M. 2009, *A&A*, 505, 859

Appendix A: RV time series and periodograms

This appendix contains figures with the radial-velocity time series and respective GLS periodogram for each star.

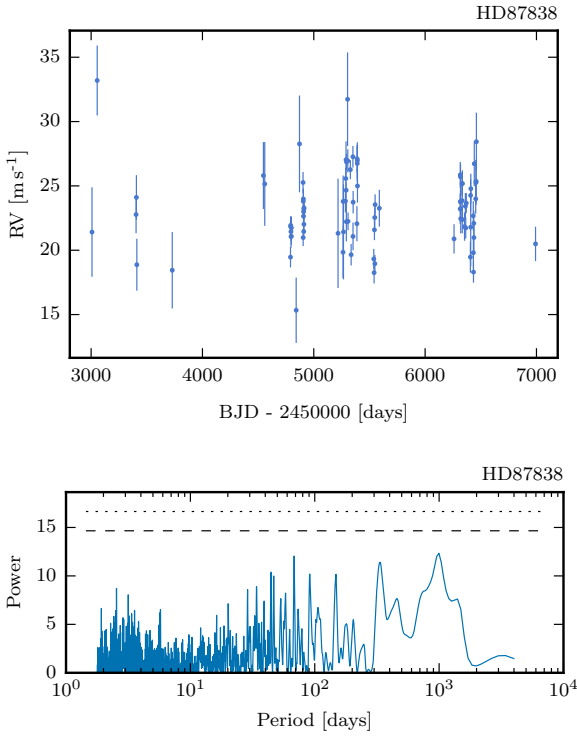


Fig. A.1. Radial-velocity time series and periodogram for HD87838.

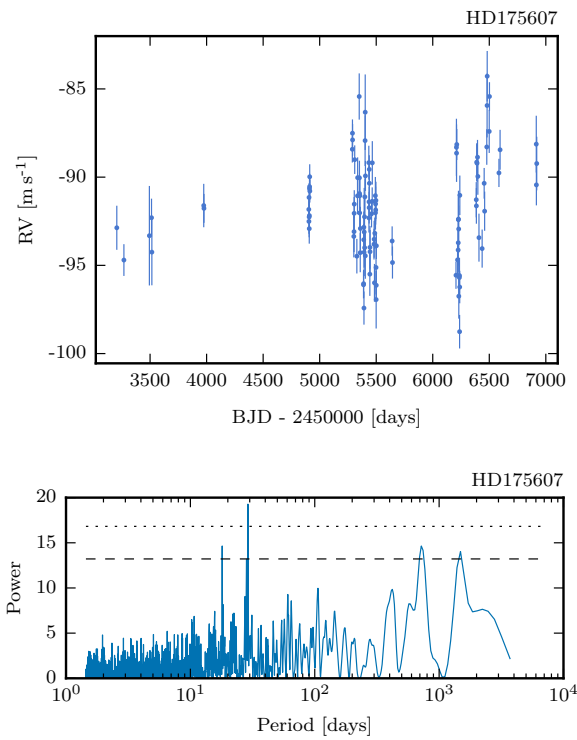


Fig. A.2. Radial-velocity time series and periodogram for HD175607.

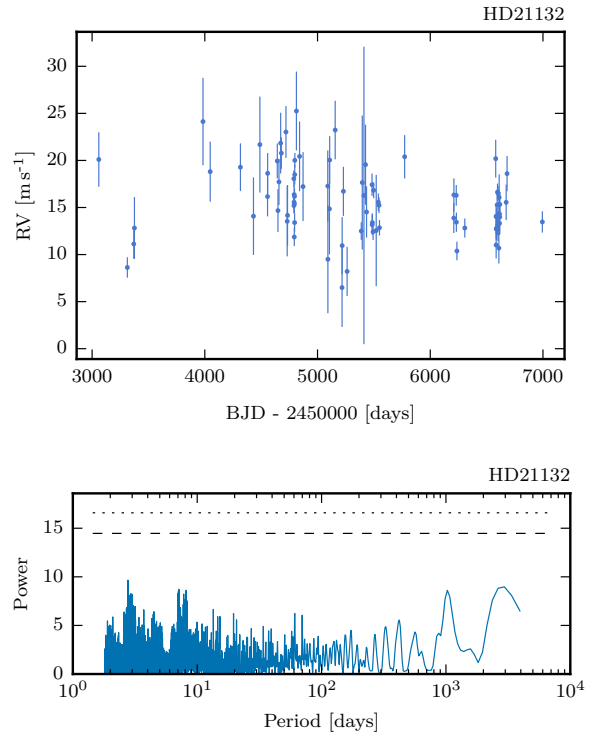


Fig. A.3. Radial-velocity time series and periodogram for HD21132.

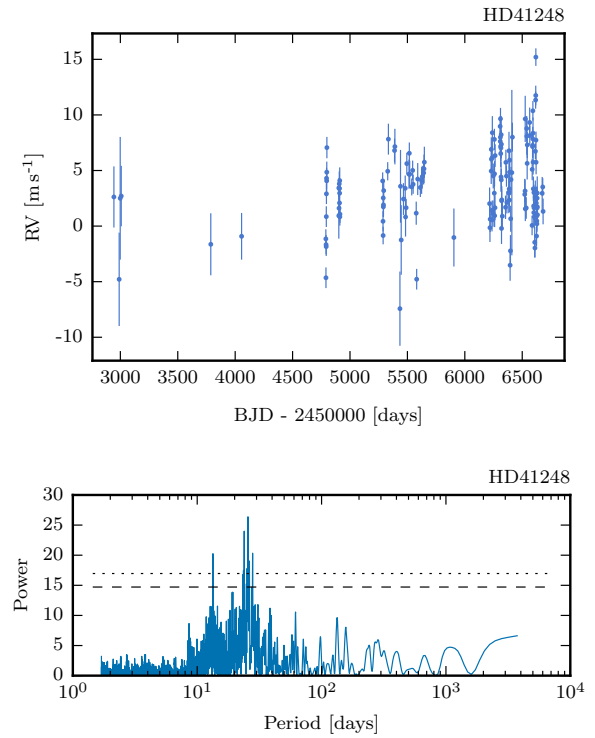


Fig. A.4. Radial-velocity time series and periodogram for HD41248.

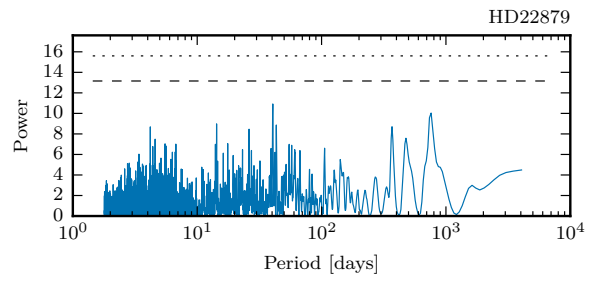
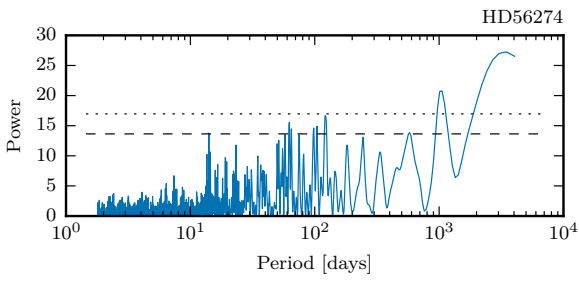
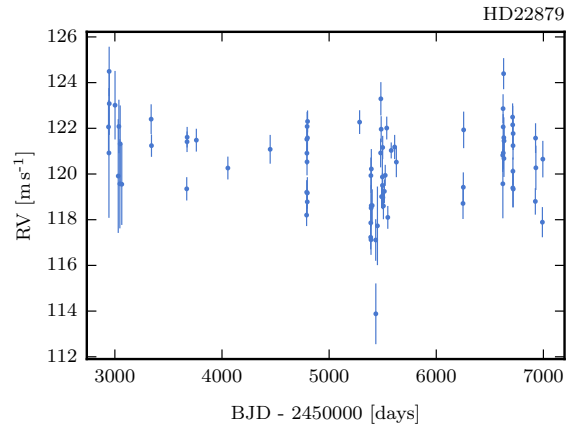
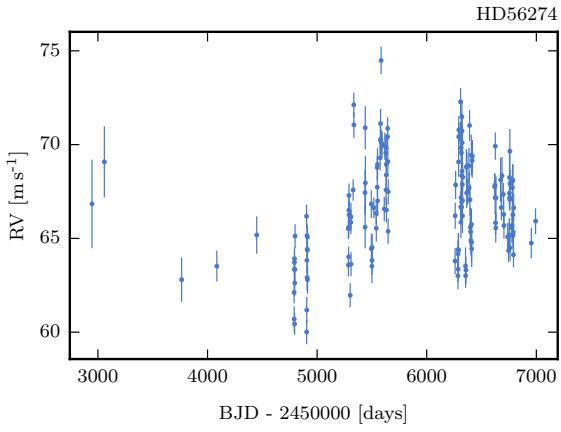


Fig. A.5. Radial-velocity time series and periodogram for HD56274.

Fig. A.7. Radial-velocity time series and periodogram for HD22879.

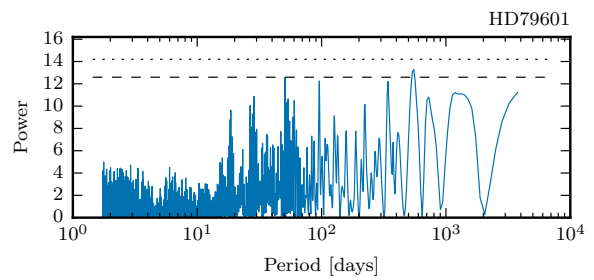
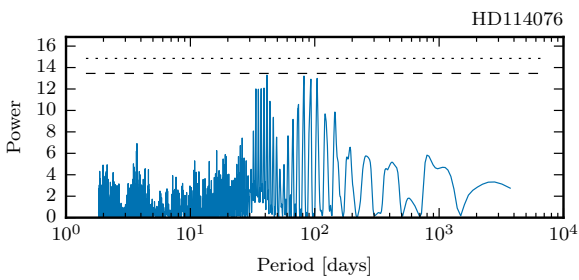
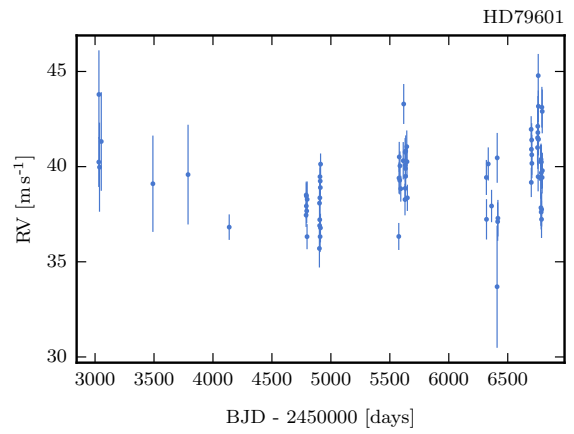
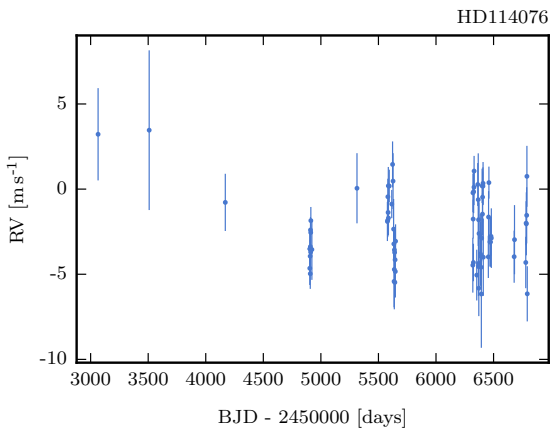


Fig. A.6. Radial-velocity time series and periodogram for HD114076.

Fig. A.8. Radial-velocity time series and periodogram for HD79601.

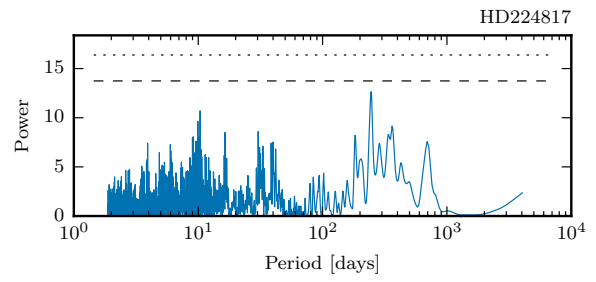
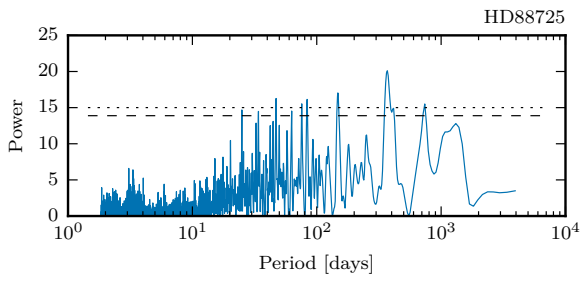
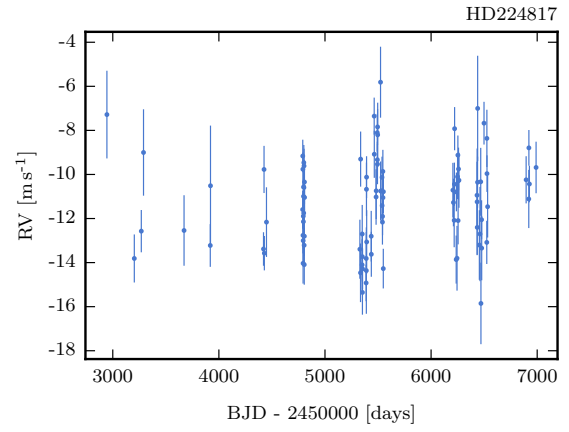
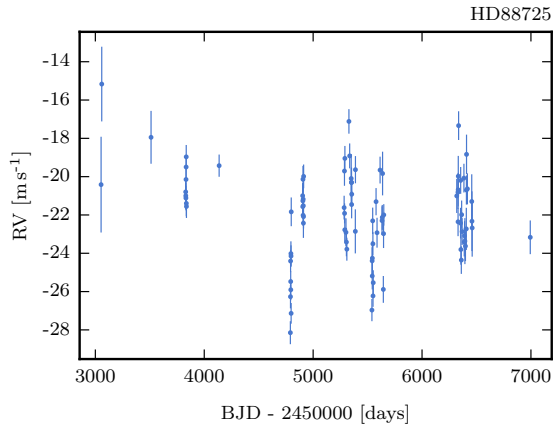


Fig. A.9. Radial-velocity time series and periodogram for HD88725.

Fig. A.11. Radial-velocity time series and periodogram for HD224817.

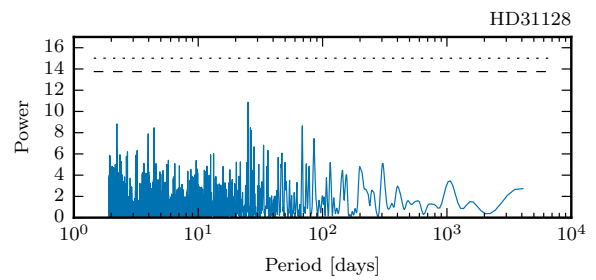
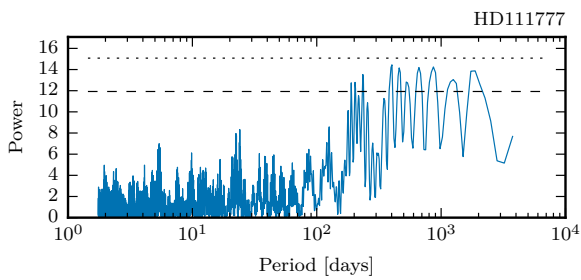
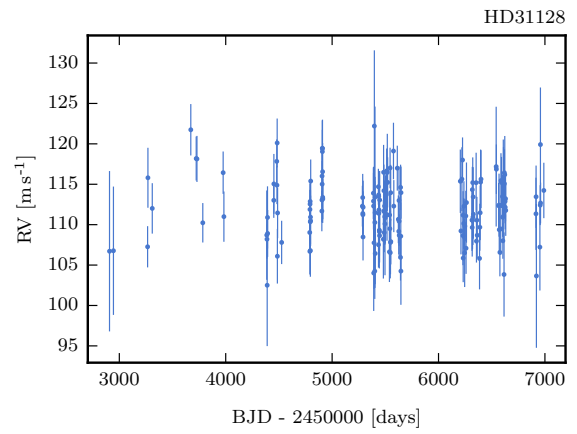
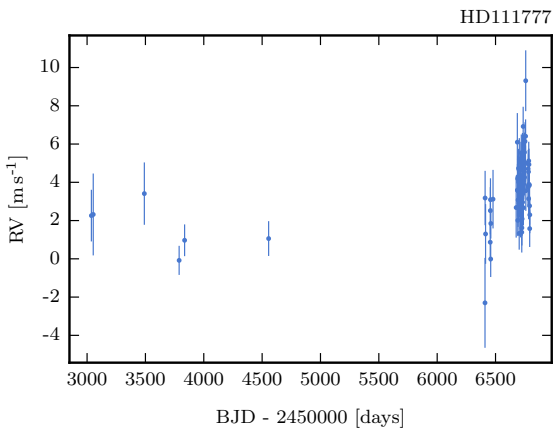


Fig. A.10. Radial-velocity time series and periodogram for HD111777.

Fig. A.12. Radial-velocity time series and periodogram for HD31128.

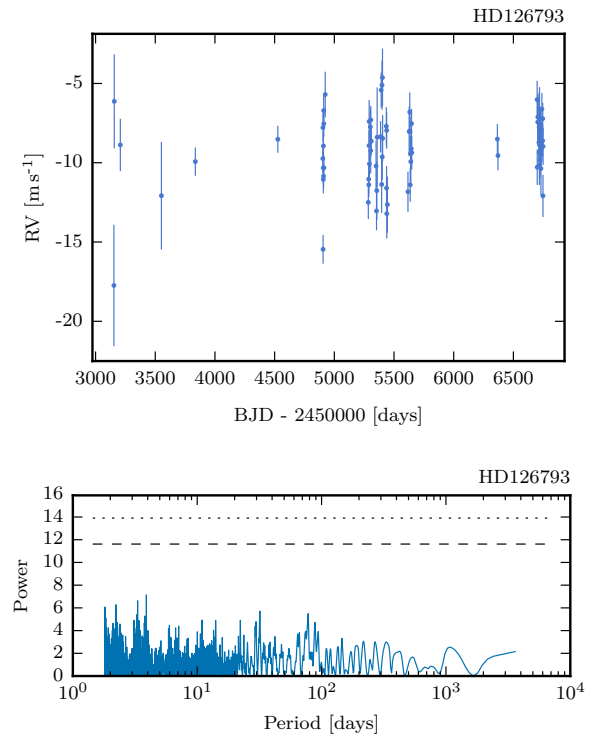
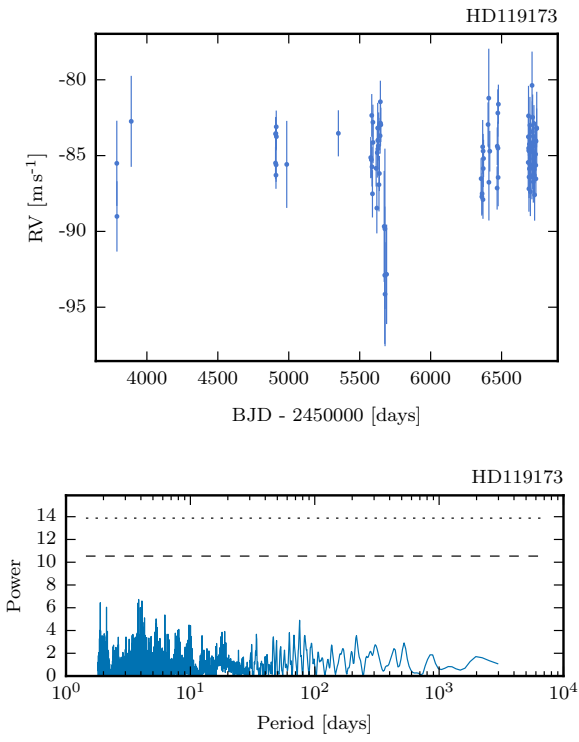


Fig. A.13. Radial-velocity time series and periodogram for HD119173.

Fig. A.15. Radial-velocity time series and periodogram for HD126793.

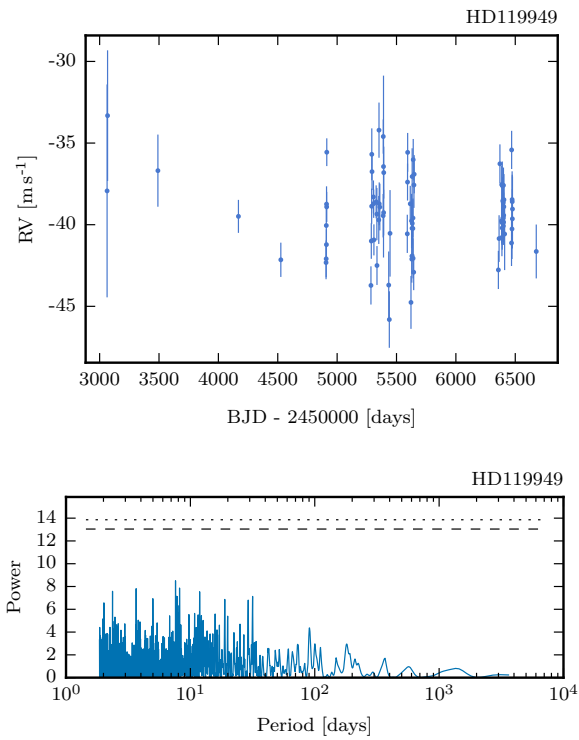


Fig. A.14. Radial-velocity time series and periodogram for HD119949.